

Power uprates
and plant life extension

CASL-U-2013-0100-000



Engineering design
and analysis

Hydra-TH: A Thermal-Hydraulics Code for Nuclear Reactor Applications

Idaho National Laboratory and Los Alamos National
Laboratory

R.R. Nourgaliev, M.A. Christon, J. Bakosi, R.B. Lowrie,
L.A. Pritchett- Sheats

May 12-17, 2013:

Science-enabling
high performance
computing

Fundamental science

Plant operational data



U.S. DEPARTMENT OF
ENERGY

Nuclear Energy

Hydra-TH: A Thermal-Hydraulics Code for Nuclear Reactor Applications

R.R. Nourgaliev

Nuclear Science & Technology, NST
Idaho National Laboratory
P.O. Box 1625, Idaho Falls, ID, 83415, USA
Robert.Nourgaliev@inl.gov

M.A. Christon, J. Bakosi, R.B. Lowrie, L.A. Pritchett-Sheats

Computational Physics & Methods, CCS-2
Los Alamos National Laboratory
Box 1663, MS D413, Los Alamos, NM, 87545, USA
{christon,jbakosi,lowrie,lpritch}@lanl.gov

KEY WORDS

Computational Fluid Dynamics, Multiphase Flows, Non-Linear Solvers, Turbulence Modeling, Grid-to-Rod Fretting

ABSTRACT

Hydra-TH is a hybrid finite-volume/finite-element multi-physics code that is being developed for the Consortium for Advanced Simulation of Light-Water Reactors to solve thermal-hydraulics problems in nuclear reactors. The thermal-hydraulics applications include crud-induced power shift and localized corrosion, grid-to-rod fretting (GTRF), sub-cooled boiling, and departure from nucleate boiling. Understanding these problems through computer simulations requires advanced, high-fidelity modeling capabilities for single and multi-phase turbulent flows. A high-level overview of Hydra-TH is given with some details on algorithms and solution strategies for both single and multi-phase flows, available turbulence models, and a validation & verification strategy. An example GTRF simulation of a single-phase turbulent flow in a reactor-core sub-assembly is also discussed.

1 INTRODUCTION

There are several challenging problems vendors and plant operators face when designing and operating nuclear reactors, e.g., *Crud-Induced Power Shift* (CIPS), *Crud-Induced Localized Corrosion* (CILC), *Grid-To-Rod Fretting* (GTRF), and *Departure from Nucleate Boiling* (DNB). The Consortium for Advanced Simulation of Light-Water Reactors (CASL) was formed to create state-of-the-art computational technologies, developed within the U.S. Department of Energy, for the modeling and simulation of commercial nuclear reactors. Computer simulation of the engineering problems in nuclear reactors require an accurate representation of different physical phenomena coupled at multiple length and time scales. Single- and multi-phase thermal-hydraulics is one of the key ingredients of a successful simulation capability for these engineering problems that provides the thermal and structural loads on fuel assemblies, and the transport and deposition of corrosion products and boron inside a reactor core.

Various computational tools have been developed and used for the analysis of reactor thermal-hydraulics. These include both specialized reactor safety codes (e.g. RELAP5,

TRACE, TRAC, RETRAN, and CATHARE), and commercial computational fluid dynamics packages (e.g. CFX, Fluent, STAR-CD, and STAR-CCM+). The focus within CASL is on developing a computational capability that enables the simulation of the thermal-hydraulics processes inside a nuclear reactor at unprecedented fidelity. These simulations can use tens of thousands of compute cores on the largest supercomputers in the world and enable the detailed resolution of turbulent flow fields and their interaction with the reactor fuel assembly. The ultimate goal is to increase our understanding of the physics of the key challenge problems and enable the development of specialized engineering models used in the design of next-generation nuclear power plants.

Hydra-TH is a multi-physics code being developed at Los Alamos National Laboratory to provide the thermal-hydraulics capability in the simulation of the challenge problems discussed above. This paper gives an overview of the current capabilities and the development status. We start with a short description of two of the solution algorithms available in Hydra-TH, in §2, followed by an overview of the turbulence modeling capabilities, §3, then the status of the multi-phase models and solvers is given in §4. The code verification and validation strategy is described in §5. A brief overview of an application of Hydra-TH to the GTRF problem is discussed in §6. Summary and pointers to future work are given in §7.

2 SOLUTION ALGORITHMS FOR SINGLE-PHASE FLOW

Hydra-TH uses pressure-based projection algorithms for flow problems at low or moderate Mach numbers. Projection algorithms are considered to be the most efficient for numerically computing incompressible flows in a time-accurate manner. In this section, two solution algorithms are presented that are used for computing the solution of the incompressible Navier-Stokes equations governing single-phase flows. After a brief description of the governing equations and their boundary conditions, §2.1–§2.2, a semi-implicit, §2.3, and a fully implicit, §2.4, projection algorithm are given.

2.1 Governing Equations for Single-Phase Flow

Incompressible single-phase flows are computed by solving the conservation equations of mass, momentum, and energy. The conservation of linear momentum is

$$\rho \left\{ \frac{\partial \mathbf{v}}{\partial t} + \mathbf{v} \cdot \nabla \mathbf{v} \right\} = \nabla \cdot \boldsymbol{\sigma} + \mathbf{f} \quad (1)$$

where $\mathbf{v} = (v_x, v_y, v_z)$ is the velocity, $\boldsymbol{\sigma}$ is the stress tensor, ρ is the mass density, and \mathbf{f} is the body force. The body force contribution \mathbf{f} typically accounts for buoyancy forces. The stress may be written in terms of the fluid pressure and the deviatoric stress tensor as $\boldsymbol{\sigma} = -p\mathbf{I} + \boldsymbol{\tau}$, where p is the pressure, \mathbf{I} is the identity tensor, and $\boldsymbol{\tau}$ is the deviatoric stress. A constitutive equation relates the deviatoric stress and the strain as $\boldsymbol{\tau} = 2\mu\mathbf{S}$. The strain-rate tensor is written in terms of the velocity gradients as $\mathbf{S} = (\nabla \mathbf{v} + (\nabla \mathbf{v})^T)/2$. In the incompressible limit, the velocity field is solenoidal,

$$\nabla \cdot \mathbf{v} = 0 \quad (2)$$

which acts as a constraint on the momentum equation (1).

Conservation of energy is expressed in terms of temperature ¹, T , as

$$\rho C_p \left\{ \frac{\partial T}{\partial t} + \mathbf{v} \cdot \nabla T \right\} = -\nabla \cdot \mathbf{q} + q''' \quad (3)$$

where C_p is the specific heat at constant pressure, \mathbf{q} is the diffusional heat flux, and q''' represents volumetric heat sources and sinks, e.g., due to chemical reactions. Fourier's law relates the heat flux to the temperature gradient and thermal conductivity as $\mathbf{q} = -\kappa \nabla T$, where κ is the thermal conductivity.

2.2 Boundary and Initial Conditions for Single-Phase Flow

The numerical solution of the constrained system of partial differential equations, Eqs. (1–3), require appropriate boundary and initial conditions. Boundary conditions, specified for a flow domain, are either physical or implied for the purposes of performing a simulation.

The momentum equation (1) is subject to boundary conditions that consist of specified velocity, $\hat{\mathbf{v}}$, on Γ_1 ,

$$\mathbf{v}(\mathbf{x}, t) = \hat{\mathbf{v}}(\mathbf{x}, t) \text{ on } \Gamma_1 \quad (4)$$

or specified traction, $\hat{\mathbf{f}}$, on Γ_2 ,

$$\boldsymbol{\sigma} \cdot \mathbf{n} = \{-p\mathbf{I} + 2\mu\mathbf{S}\} \cdot \mathbf{n} = \hat{\mathbf{f}}(\mathbf{x}, t) \text{ on } \Gamma_2 \quad (5)$$

where $\Gamma = \Gamma_1 \cup \Gamma_2$ is the complete domain boundary, and the outward normal is \mathbf{n} . In the case of a no-slip and no-penetration boundary, $\mathbf{v} = 0$ is prescribed. The traction and velocity boundary conditions can be mixed. For example, in a two-dimensional sense, mixed boundary conditions can consist of a prescribed normal traction and a tangential velocity. A detailed discussion of boundary conditions for the incompressible Navier-Stokes equations may be found in Gresho and Sani [12].

The boundary conditions for the energy equation (3), can be a prescribed temperature,

$$T(\mathbf{x}, t) = \hat{T}(\mathbf{x}, t) \quad (6)$$

or prescribed heat flux,

$$-\kappa \nabla T \cdot \mathbf{n} = \hat{q}(\mathbf{x}, t) \quad (7)$$

where \hat{q} is the known flux through the boundary with normal \mathbf{n} . The heat flux may also be prescribed in terms of a heat transfer coefficient, h , and a reference temperature, T_∞ ,

$$-\kappa \nabla T \cdot \mathbf{n} = h(T - T_\infty) \quad (8)$$

The initial conditions prescribe velocity and temperature at $t = 0$, i.e.,

$$\begin{aligned} \mathbf{v}(\mathbf{x}, 0) &= \mathbf{v}^0(\mathbf{x}) \\ T(\mathbf{x}, 0) &= T^0(\mathbf{x}). \end{aligned} \quad (9)$$

¹The energy equation can be solved also in terms of specific internal energy u or specific enthalpy h based on user-defined input.

Remark 1 For a well-posed incompressible flow problem, the prescribed initial velocity field in Eq. (9) must satisfy Eqs. (10) and (11), see [15]. If $\Gamma_2 = \emptyset$ (the null set, i.e., enclosure flows with $\mathbf{n} \cdot \mathbf{v}$ prescribed on all surfaces), then global mass conservation enters as an additional solvability constraint as shown in Eq. (12),

$$\nabla \cdot \mathbf{v}^0 = 0 \quad (10)$$

$$\mathbf{n} \cdot \mathbf{v}(\mathbf{x}, 0) = \mathbf{n} \cdot \mathbf{v}^0(\mathbf{x}) \quad (11)$$

$$\int_{\Gamma} \mathbf{n} \cdot \mathbf{v}^0 d\Gamma = 0 \quad (12)$$

2.3 Semi-Implicit Second-Order Projection for Single-Phase Flow

The starting point for the semi-implicit projection method is Gresho’s second-order “P2” method [13, 14], which is closely related to [2]. A discontinuous-Galerkin/finite-volume (DG/FV) formulation ensures local, i.e., cell-wise, conservation. The velocity, temperature (internal energy or enthalpy), and turbulence variables (e.g. k , ϵ , ω , etc. if a turbulence model is used) are cell-centered, while the pressure is centered at nodes of the computational mesh. The node-centered pressure precludes checker-board modes, which avoids the use of troublesome pressure-stabilization techniques, e.g., Rhie-Chow filtering. Thus, a hybrid DG/FV – Galerkin FEM method forms the basis for the Hydra-TH incompressible solution algorithms.

Hybrid discretization for projection methods is not new. The first use of an FV scheme with a continuous-Galerkin pressure-Poisson operator appeared in the work of Bell, et al. [2] on structured meshes. More recently, Aliabadi and co-workers have developed a hybrid FE/FV method [24, 25, 26], that is similar to the methods presented here.

The governing equations presented in §2.1 serve as the starting point for the development of the hybrid solution method. We use vector notation and write the stress in terms of fluid pressure and the deviatoric stress, $\boldsymbol{\sigma} = -p\mathbf{I} + \boldsymbol{\tau}$, and the advective terms in divergence form. Following the procedure outlined in Chapter 7 of the Hydra-TH theory manual [4], we discretize in space, integrate by parts, and apply the divergence theorem.

$$\rho \frac{d}{dt} \int_{\Omega^e} \mathbf{v} d\Omega^e + \oint_{\Gamma^e} \rho \mathbf{v} (\mathbf{v} \cdot \mathbf{n}) d\Gamma^e - \oint_{\Gamma^e} \boldsymbol{\tau} \cdot \mathbf{n} d\Gamma^e + \int_{\Omega^e} \nabla p d\Omega^e - \int_{\Omega^e} \mathbf{f} d\Omega^e = 0 \quad (13)$$

Using the definition for the cell-average, $\bar{\mathbf{v}} = \frac{1}{\Omega^e} \int_{\Omega^e} \mathbf{v}^h$, where Ω^e is the element volume, the spatially-discrete momentum equations become

$$\rho \Omega^e \frac{d\bar{\mathbf{v}}}{dt} + \oint_{\Gamma^e} \rho \mathbf{v} (\mathbf{v} \cdot \mathbf{n}) d\Gamma^e - \oint_{\Gamma^e} \boldsymbol{\tau} \cdot \mathbf{n} d\Gamma^e + \int_{\Omega^e} \nabla p d\Omega^e - \int_{\Omega^e} \mathbf{f} d\Omega^e = 0 \quad (14)$$

The requirement for a divergence-free velocity field, Eq. (2) constrains Eq. (14) and yield a system of differential algebraic equations (DAE) not ordinary differential equations (ODE). As a result, traditional time-marching schemes can not be applied to the div-constrained system of equations.

A projection algorithm can be derived in a number of ways. We first develop the time-integrator and identify the terms associated with the projection via a Helmholtz decomposition of the velocity field. The element-level mass, advective, viscous, gradient, and body-force operators are defined respectively as

$$M^e = \rho \Omega^e \quad (15)$$

$$A^e(\rho, \mathbf{v})\mathbf{v} = \oint_{\Gamma^e} \rho \mathbf{v} (\mathbf{v} \cdot \mathbf{n}) d\Gamma^e \quad (16)$$

$$K^e \mathbf{v} = \oint_{\Gamma^e} \boldsymbol{\tau} \cdot \mathbf{n} d\Gamma^e \quad (17)$$

$$\mathbf{B}^e p \Omega^e = \int_{\Omega^e} \nabla p d\Omega^e \quad (18)$$

$$\mathbf{F}^e = \int_{\Omega^e} \mathbf{f} d\Omega^e \quad (19)$$

Applying the forward and backward Euler schemes to Eq. (14) with explicit advection, then taking the θ -weighted sum of the fully-discrete systems gives

$$M \frac{\bar{\mathbf{v}}^{n+1} - \bar{\mathbf{v}}^n}{\Delta t} - \theta K \bar{\mathbf{v}}^{n+1} = (1 - \theta) \mathbf{F}^n + \theta \mathbf{F}^{n+1} - A(\rho, \bar{\mathbf{v}}) \bar{\mathbf{v}}^n + (1 - \theta) K \bar{\mathbf{v}}^n - \mathbf{B} \bar{p}^n - \theta_p \mathbf{B} (\bar{p}^{n+1} - \bar{p}^n) \quad (20)$$

where $0 \leq \theta \leq 1$, i.e., $\theta = 0$ corresponds to forward Euler, $\theta = 1/2$ to the trapezoidal rule, while $\theta = 1$ gives backward Euler for the viscous and body-force terms. Here, M , K , A , B and F indicate global operators assembled over all elements.

Remark 2 For clarity, the formulation is presented here with explicit advection. A detailed discussion of advection methods is beyond the scope of this paper. In Hydra-TH, the advection is implemented using a linearized monotonicity-preserving advection operator with the primitive variables, i.e. velocity, temperature (enthalpy or internal energy), etc., treated implicitly. This provides unconditional stability for (linear) scalar transport equations, and conditional but relaxed stability for the non-linear momentum equations. Although a sharp estimate is not available for the momentum equations, experience shows that $5 \leq CFL \leq 10$ remains stable for time-accurate problems, while a significantly larger CFL is possible when pseudo-time marching is used for steady-state problems.

Following the time-discretization, the velocity field is decomposed into divergence-free and curl-free parts,

$$\bar{\mathbf{v}}^* = \bar{\mathbf{v}}^{n+1} + \frac{1}{\rho} \nabla \lambda \quad (21)$$

with the Lagrange multiplier,

$$\lambda = \theta_p \Delta t (\bar{p}^{n+1} - \bar{p}^n) \quad (22)$$

Substituting Eq. (21) for $\bar{\mathbf{v}}^{n+1}$ into Eq. (20), using Eq. (22), and assuming $K \nabla \lambda = 0$ everywhere inside Ω , the momentum equation is solved for $\bar{\mathbf{v}}^*$ as

$$[M - \theta \Delta t K] \bar{\mathbf{v}}^* = [M + (1 - \theta) \Delta t K] \bar{\mathbf{v}}^n - \Delta t A(\rho, \bar{\mathbf{v}}) \bar{\mathbf{v}}^n - \Delta t \mathbf{B} \bar{p}^n + \Delta t \{(1 - \theta) \mathbf{F}^n + \theta \mathbf{F}^{n+1}\} \quad (23)$$

Requiring $\nabla \cdot \bar{\mathbf{v}}^{n+1} = 0$ in the Helmholtz decomposition, Eq. (21), yields the pressure-Poisson equation (PPE) that is solved for the Lagrange multiplier, λ ,

$$\nabla \cdot \frac{1}{\rho} \nabla \lambda = \nabla \cdot \bar{\mathbf{v}}^* \quad (24)$$

The Galerkin finite element procedure is then used to discretize Eq. (24) for the node-centered λ ,

$$\int_{\Omega} \nabla w \cdot \left(\frac{1}{\rho} \nabla \lambda \right) d\Omega = \int_{\Gamma} w \left\{ \frac{1}{\rho} \frac{\partial \lambda}{\partial n} \right\} - \int_{\Gamma} w \bar{\mathbf{v}}^* \cdot \mathbf{n} d\Gamma + \int_{\Omega} \bar{\mathbf{v}}^* \cdot \nabla w d\Omega \quad (25)$$

yielding the discretized PPE

$$K_p \lambda = D \quad (26)$$

Here, K_p and D are global, i.e., have been assembled over all elements.

Remark 3 An alternative formulation for the PPE may use the cell-centered divergence of $\bar{\mathbf{v}}^*$ for $\int_{\Omega} \nabla \cdot \bar{\mathbf{v}}^*$ in Eq. (24). This cell-centered form leads to smoother pressure fields, however, it may result in initial velocity and pressure fields that less accurate than those obtained with Eq. (25).

Given the velocity and pressure at time-level n , the projection algorithm follows the steps below to compute time-level $(n + 1)$.

Algorithm 1 P2 Projection

1. Solve for $\bar{\mathbf{v}}^*$

$$[M - \theta \Delta t K] \bar{\mathbf{v}}^* = [M + (1 - \theta) \Delta t K] \bar{\mathbf{v}}^n - \Delta t A(\rho, \bar{\mathbf{v}}) \bar{\mathbf{v}}^n - \Delta t \mathbf{B} \bar{p}^n + \Delta t \{ (1 - \theta) \mathbf{F}^n + \theta \mathbf{F}^{n+1} \} \quad (27)$$

2. Compute the right-hand-side of the PPE and solve for λ ,

$$K_p \lambda = D \quad (28)$$

3. Update the pressure²

$$\bar{p}^{n+1} = \bar{p}^n + \frac{1}{\theta_p \Delta t} \lambda \quad (29)$$

4. Project the cell-centered velocities

$$\bar{\mathbf{v}}^{n+1} = \bar{\mathbf{v}}^* - \frac{1}{\rho} \mathbf{B} \lambda \quad (30)$$

5. Compute face gradients and project the face-centered velocities

$$v_f = v_f^* - \frac{1}{\rho_f} ((\mathbf{B}) \lambda)_f \cdot \mathbf{n} \quad (31)$$

²Testing over the past 20 years has indicated that $\theta_p = 1/2$ in Eq. (29) can lead to temporal oscillations in the pressure. For this reason, we use $\theta_p = 1$ in Hydra-TH.

2.4 Fully Implicit Second-Order Projection for Single-Phase Flow

We now extend the semi-implicit projection method, discussed in §2.3, to a fully implicit algorithm using Picard and Newton based iterative methods using the projection method as a physics-based preconditioner. For clarity, we only discuss momentum and mass, i.e., velocity-pressure coupling, and note that the extension to include the energy equation and turbulence model equations is straightforward.

The governing equations are Eqs. (1) and (2), as before, and the vectors of unknowns are either

$$\mathbf{U} = \begin{bmatrix} \bar{p} \\ \bar{\mathbf{v}} \end{bmatrix} \quad \text{or} \quad \mathbf{W} = \begin{bmatrix} \lambda \\ \bar{\mathbf{v}}^* \end{bmatrix} \quad (32)$$

The fully-implicit algorithm seeks the solution at t^{n+1} iteratively, by updating $\mathbf{U}^{\diamond\diamond}$ or $\mathbf{W}^{\diamond\diamond}$ as

$$\begin{aligned} \lambda^{\diamond\diamond} &= \lambda^{\diamond} + \lambda' \\ \bar{p}^{\diamond\diamond} &= \bar{p}^{\diamond} + p' \\ \bar{\mathbf{v}}^{\diamond\diamond} &= \bar{\mathbf{v}}^{\diamond} + \mathbf{v}' \\ \bar{\mathbf{v}}^{*\diamond\diamond} &= \bar{\mathbf{v}}^{*\diamond} + \mathbf{v}^{*\prime} = \bar{\mathbf{v}}^{\diamond\diamond} + 1/\rho \nabla \lambda^{\diamond\diamond} \end{aligned} \quad (33)$$

We linearize the body force as

$$\mathbf{F}^{\diamond\diamond} = \mathbf{F}^{\diamond} + \mathbb{F}_{\mathbf{v}} \left(\mathbf{U}^{\diamond} \right) \mathbf{v}' + \mathbf{f}_p \left(\mathbf{U}^{\diamond} \right) p' \quad (34)$$

where specific forms of the linearization matrix $\mathbb{F}_{\mathbf{v}}$ and vector \mathbf{f}_p are problem-dependent.

Picard-based algorithm. Substituting Eq. (33) into Eq. (27) yields

$$\begin{aligned} M \frac{\bar{\mathbf{v}}^{*\diamond\diamond} - \bar{\mathbf{v}}^n}{\Delta t} &= (1 - \theta) \left(K \bar{\mathbf{v}}^n - A(\rho, \bar{\mathbf{v}}^n) \bar{\mathbf{v}}^n + \mathbf{F}^n \right) - \mathbf{B} \bar{p}^n + \\ &\quad + \theta \left\{ \left[K - A(\rho, \bar{\mathbf{v}}^{\diamond}) \right] \bar{\mathbf{v}}^{*\diamond\diamond} + \mathbf{F}^{\diamond} - \underbrace{\left[K - A(\rho, \bar{\mathbf{v}}^{\diamond}) \right] \left(\frac{1}{\rho} \nabla \lambda^{\diamond} \right)}_{\Xi_t} \right\} \\ &\quad - \theta \left\{ \underbrace{\left[K - A(\rho, \bar{\mathbf{v}}^{n+1}) \right] \left(\frac{1}{\rho} \nabla \lambda' \right) + \frac{1}{\theta_p \Delta t} \mathbf{f}_p \lambda' + \mathbb{F}_{\mathbf{v}} \mathbf{v}'}_{\delta \mathcal{J}_{\mathbf{v}}} \right\} \end{aligned} \quad (35)$$

Compared to Eq.(27) we have the additional terms:

$$\mathbf{m}' = -\theta (\Xi_t + \delta \mathcal{J}_{\mathbf{v}}) \quad (36)$$

after which Eq. (35) can be written as

$$\begin{aligned} \left[M - \theta \Delta t \left(K - A \left(\rho, \bar{\mathbf{v}}^{\diamond} \right) \right) \right] \bar{\mathbf{v}}^{*\diamond\diamond} &= [M + (1 - \theta) \Delta t (K - A(\rho, \bar{\mathbf{v}}^n))] \bar{\mathbf{v}}^n + \\ &\quad + \Delta t \left((1 - \theta) \mathbf{F}^n + \theta \mathbf{F}^{\diamond} - \mathbf{B} \bar{p}^n - \theta \delta \tilde{A} \bar{\mathbf{v}}^{\diamond} + \mathbf{m}' \right) \end{aligned} \quad (37)$$

where $\delta\tilde{A}\bar{\mathbf{v}}^\diamond$ denotes the linearization for the quadratic advection terms, whose details are omitted for brevity. Now the Helmholtz decomposition becomes

$$\bar{\mathbf{v}}^{*\diamond\diamond} = \underbrace{\bar{\mathbf{v}}^\diamond + \bar{\mathbf{v}}'}_{\bar{\mathbf{v}}^{\diamond\diamond}} + \frac{1}{\rho} \nabla (\lambda^\diamond + \lambda') \quad (38)$$

which yields the PPE

$$\nabla \cdot \frac{1}{\rho} \nabla \lambda^{\diamond\diamond} = \nabla \cdot \bar{\mathbf{v}}^{*\diamond\diamond} \quad (39)$$

which is the same as Eq.(24). The fixed-point iteration algorithm is based on Eqs. (37–39):

Algorithm 2 Picard Iteration

1. Set initial guess for $m = 0$:

$$\begin{array}{lll} \bar{\mathbf{v}}^\diamond & = & \bar{\mathbf{v}}^n \\ \bar{p}^\diamond & = & \bar{p}^n \\ \lambda^\diamond & = & 0 \end{array} \quad \begin{array}{lll} \mathbf{v}' & = & 0 \\ p' & = & 0 \\ \lambda' & = & 0 \end{array}$$

2. Start the m^{th} iteration.

3. Solve for $\bar{\mathbf{v}}^{*\diamond\diamond}$, Eq.(37), with $\delta\mathcal{J}_v = 0$.

4. Compute face-centered velocities, v_f^* .

5. Compute the right-hand-side of Eq. (39) and solve for $\lambda^{\diamond\diamond}$,

$$K_p \lambda^{\diamond\diamond} = D^{\diamond\diamond} \quad (40)$$

6. Update the pressure

$$\bar{p}^{\diamond\diamond} = \bar{p}^n + \frac{1}{\theta_p \Delta t} \lambda^{\diamond\diamond} \quad (41)$$

7. Project the cell-centered velocities

$$\bar{\mathbf{v}}^{\diamond\diamond} = \bar{\mathbf{v}}^* - \frac{1}{\rho} \mathbf{B} \lambda^{\diamond\diamond} \quad (42)$$

8. Compute face gradients and project the face-centered velocities

$$v_f = v_f^* - \frac{1}{\rho_f} ((B) \lambda^{\diamond\diamond})_f \cdot \mathbf{n} \quad (43)$$

9. Compute velocity and pressure corrections,

$$\begin{aligned}\mathbf{v}' &= \bar{\mathbf{v}}^{\diamond\diamond} - \bar{\mathbf{v}}^{\diamond} \\ \lambda' &= \lambda^{\diamond\diamond} - \lambda^{\diamond}\end{aligned}\quad (44)$$

and compute errors

$$\begin{aligned}\mathcal{E}_{\mathbf{v}}^{(m)} &= \mathcal{L}_2(\mathbf{v}') \\ \mathcal{E}_{\lambda}^{(m)} &= \mathcal{L}_2(\lambda')\end{aligned}\quad (45)$$

10. Check convergence: **If** any of

$$\begin{aligned}\mathcal{E}_{\mathbf{v}}^{(m)} &< \text{tol}_a \\ \mathcal{E}_{\lambda}^{(m)} &< \text{tol}_a \\ \mathcal{E}_{\mathbf{v}}^{(m)} &< \text{tol}_r \mathcal{E}_{\mathbf{v}}^{(0)} \\ \mathcal{E}_{\lambda}^{(m)} &< \text{tol}_r \mathcal{E}_{\lambda}^{(0)}\end{aligned}\quad (46)$$

are not satisfied, start a new Picard iteration: increment m , $\bar{\mathbf{v}}^{\diamond} = \bar{\mathbf{v}}^{\diamond\diamond}$, $\bar{p}^{\diamond} = \bar{p}^{\diamond\diamond}$, $\lambda^{\diamond} = \lambda^{\diamond\diamond}$, and repeat from Step 2, **otherwise**, finish the time step:

$$\begin{aligned}\bar{\mathbf{v}}^{n+1} &= \bar{\mathbf{v}}^{\diamond\diamond} \\ \bar{p}^{n+1} &= \bar{p}^{\diamond\diamond}\end{aligned}$$

The above projection-preconditioned Picard iteration ensures a solenoidal velocity field and satisfies momentum conservation with a prescribed tolerance. The algorithm is free of operator-splitting errors and time-centering ensures that both velocity and pressure are second-order accurate in time. The method is unconditionally stable for arbitrarily large CFL numbers. This is demonstrated in Figs. 1 and 2, where instantaneous velocity fields of $Re = 100$ vortex streets are compared as computed by the semi-implicit and the fully-implicit algorithms. The figures show that increasing the CFL number from 0.88 to 56 drives the semi-implicit algorithm unstable, while the fully implicit method remains stable, even as the Hops bifurcation is stepped over by ever larger time steps, see Fig. 2. Naturally, the fully implicit algorithm is intended for rapid convergence to steady state and not for time-accurate transients.

The above Picard algorithm may be suitable for a number of problems. However, it may take a large number of iterations for complex geometries and high Reynolds numbers, especially with stiff source terms. To further reduce the number of iterations required, a Newton-based algorithm is described next.

Newton-based algorithm. From Eq.(33) we have

$$\bar{\mathbf{v}}^{\diamond\diamond} = \bar{\mathbf{v}}^{\star\diamond\diamond} - \frac{1}{\rho} \nabla \lambda^{\diamond\diamond} = \bar{\mathbf{v}}^{\star\diamond} + \mathbf{v}^{\star'} - \frac{1}{\rho} \nabla (\lambda^{\diamond} + \lambda') \quad (47)$$

and

$$\bar{\mathbf{v}}^{\diamond} + \mathbf{v}' = \underbrace{\bar{\mathbf{v}}^{\star\diamond} - \frac{1}{\rho} \nabla \lambda^{\diamond}}_{\bar{\mathbf{v}}^{\diamond}} + \mathbf{v}^{\star'} - \frac{1}{\rho} \nabla \lambda' \quad (48)$$

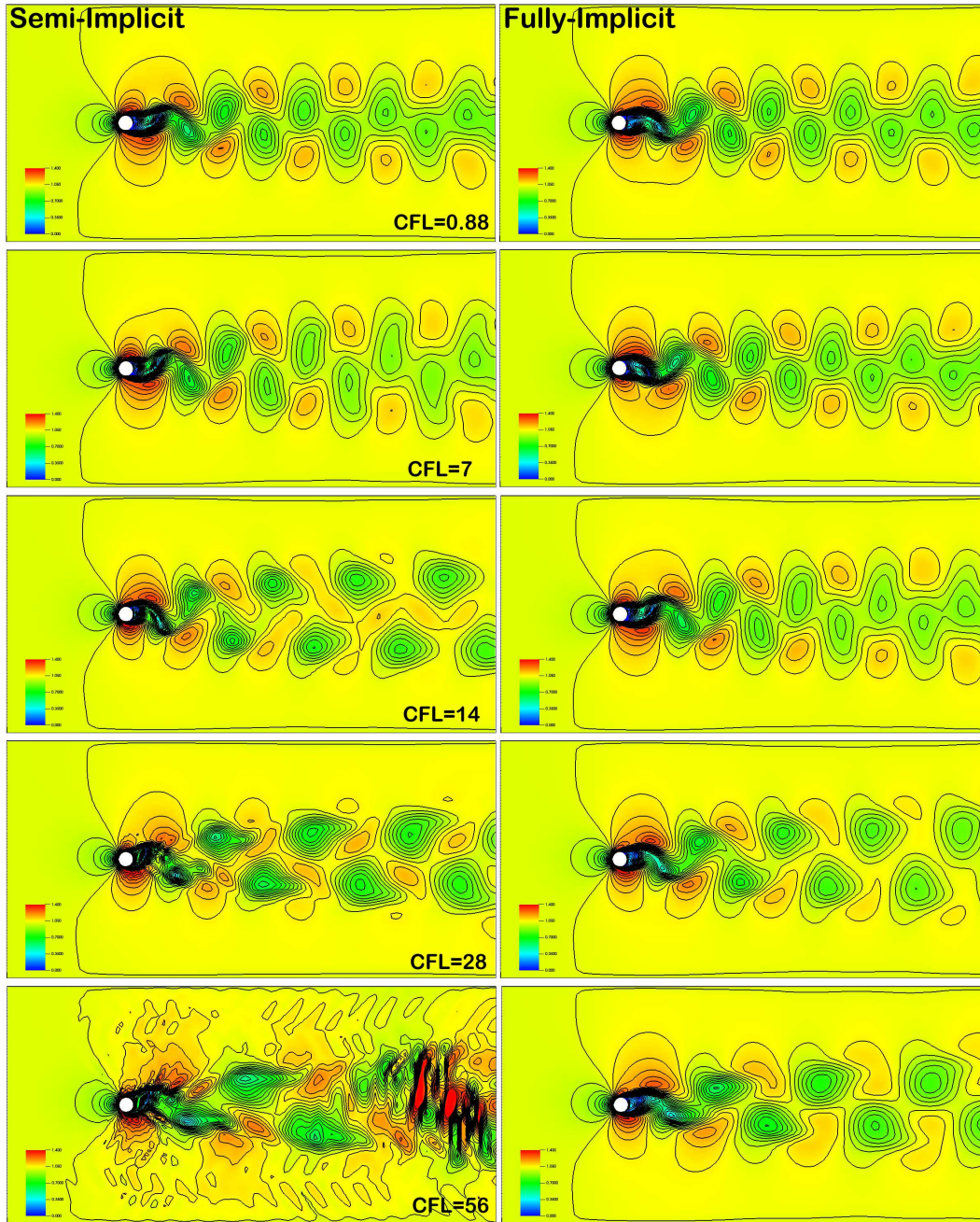


Fig. 1: Comparison of semi-implicit and fully-implicit projection, on the example of vortex shedding behind a cylinder. Velocity field for $Re = 100$.

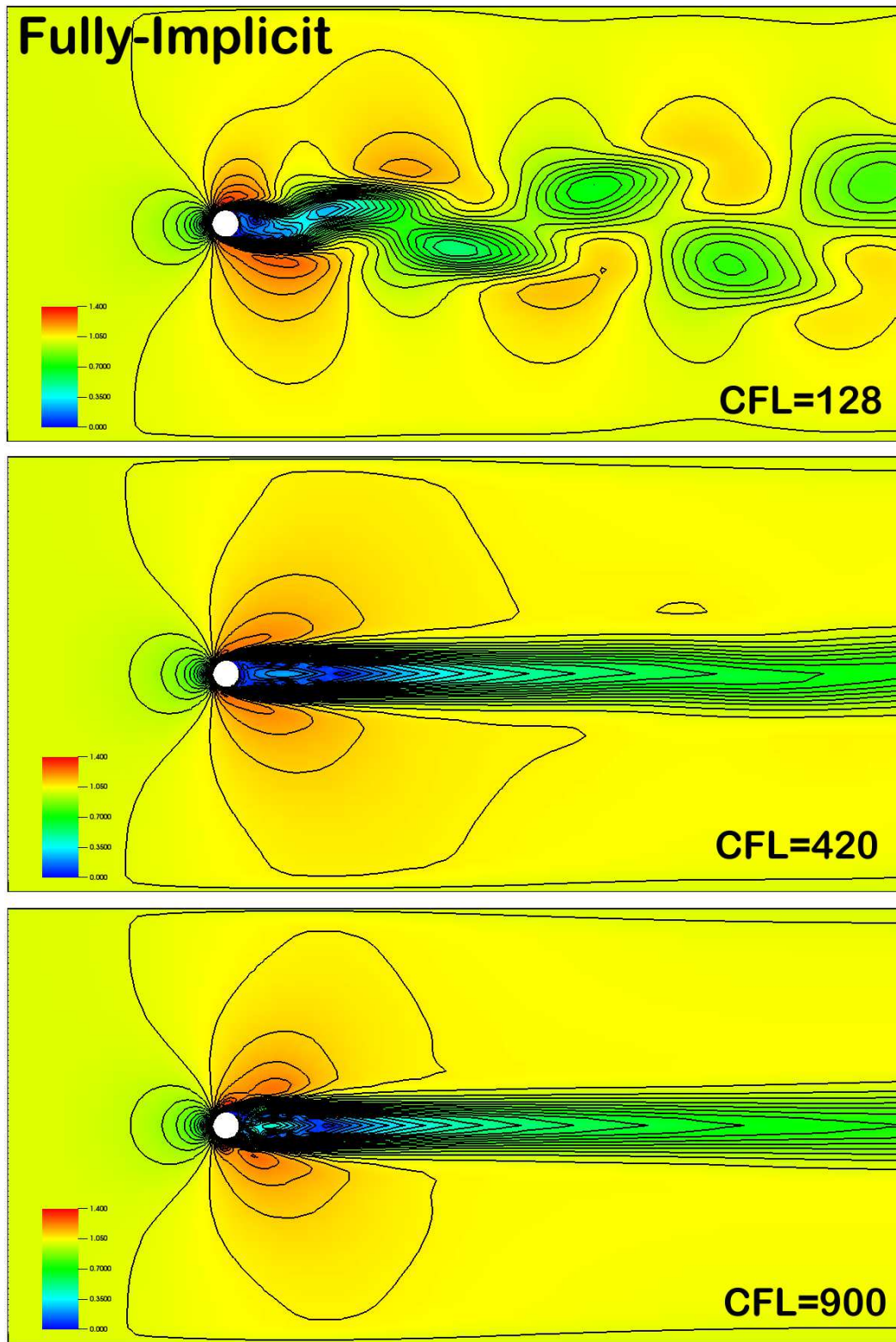


Fig. 2: Fully-implicit projection for the example of vortex shedding behind a cylinder. Velocity field for $Re = 100$. Large time step solutions.

Thus,

$$\mathbf{v}' = \mathbf{v}^{\star'} - \frac{1}{\rho} \nabla \lambda' \quad (49)$$

$$\lambda^\diamond = \theta_p \Delta t \left(\bar{p}^\diamond - \bar{p}^n \right) \quad (50)$$

$$\lambda' = \theta_p \Delta t p' \quad (51)$$

Substituting Eqs. (47–51) into Eq. (14) yields

$$\begin{aligned} & \left[\left(\Delta t \theta \left(K - A \left(\rho, \bar{\mathbf{v}}^\diamond \right) + \mathbb{F}_v \right) - M \right) \frac{1}{\rho} \nabla - \frac{\theta}{\theta_p} \mathbf{f}_p + \mathbf{B} \right] \lambda' + \\ & + \left[M - \Delta t \theta \left(K - A \left(\rho, \bar{\mathbf{v}}^\diamond \right) + \mathbb{F}_v \right) \right] \mathbf{v}^{\star'} = -\text{res}_v \end{aligned} \quad (52)$$

where

$$\begin{aligned} \text{res}_v = & M \left(\bar{\mathbf{v}}^\diamond - \bar{\mathbf{v}}^n \right) - \Delta t \left((1 - \theta) K \bar{\mathbf{v}}^n + \theta K \bar{\mathbf{v}}^\diamond \right) + \\ & + \Delta t \left((1 - \theta) A \left(\rho, \bar{\mathbf{v}}^n \right) \bar{\mathbf{v}}^n + \theta A \left(\rho, \bar{\mathbf{v}}^\diamond \right) \bar{\mathbf{v}}^\diamond \right) - \\ & - \Delta t \left((1 - \theta) \mathbf{F}^n + \theta \mathbf{F}^\diamond \right) + \Delta t \left(\mathbf{B} \bar{p}^n + \theta_p \mathbf{B} (\bar{p}^\diamond - \bar{p}^n) \right) \end{aligned} \quad (53)$$

To derive the pressure correction (Lagrange multiplier) equation, we take the divergence of Eq.(47):

$$\cancel{\nabla \cdot \bar{\mathbf{v}}^\diamond} = \nabla \cdot \bar{\mathbf{v}}^{\star'} + \nabla \cdot \mathbf{v}^{\star'} - \nabla \cdot \frac{1}{\rho} \nabla \lambda^\diamond - \nabla \cdot \frac{1}{\rho} \nabla \lambda' \quad (54)$$

which yields the *pressure correction equation*,

$$\nabla \cdot \frac{1}{\rho} \nabla \lambda' - \nabla \cdot \mathbf{v}^{\star'} = -\text{res}_\lambda \quad (55)$$

where

$$\text{res}_\lambda = \nabla \cdot \frac{1}{\rho} \nabla \lambda^\diamond - \nabla \cdot \bar{\mathbf{v}}^{\star'} \quad (56)$$

The iterations of the linearized Newton-based algorithm are carried out on the system,

$$\underbrace{\begin{bmatrix} \nabla \cdot \frac{1}{\rho} \nabla & -\nabla \cdot \\ \left(\Delta t \theta \left(K - A \left(\rho, \bar{\mathbf{v}}^\diamond \right) + \mathbb{F}_v \right) - M \right) \frac{1}{\rho} \nabla - \frac{\theta}{\theta_p} \mathbf{f}_p + \mathbf{B} & M - \Delta t \theta \left(K - A \left(\rho, \bar{\mathbf{v}}^\diamond \right) + \mathbb{F}_v \right) \end{bmatrix}}_{\text{Jacobian, } \mathbb{J}_{\mathbf{w}}} \underbrace{\begin{bmatrix} \lambda' \\ \mathbf{v}^{\star'} \end{bmatrix}}_{\mathbf{w}'} = \underbrace{\begin{bmatrix} \text{res}_\lambda \\ \text{res}_v \end{bmatrix}}_{\text{res}_{\mathbf{v}}} \quad (57)$$

The non-linear residuals, res_λ and res_v , are supplied to PETSc-SNES using a Jacobian-Free Newton-Krylov implementation. As a (physics-based) preconditioning [17] of the linear solver (GMRES), one can apply the Picard-based projection algorithm, described above.

3 OVERVIEW OF TURBULENCE MODELING IN HYDRA-TH

Hydra-TH is designed to incorporate both well-established and state-of-the-art turbulence models, ranging from Reynolds-averaged Navier-Stokes (RANS) models to large-eddy simulation (LES) techniques to various hybrid RANS-LES models. RANS models include the Spalart-Allmaras model and various flavors of turbulent-viscosity models (e.g. k - ϵ , k - ω). Available LES and hybrid RANS-LES variants include the monotonically integrated (or implicit) LES model, and different explicit treatments for the unresolved scales, e.g. the Smagorinsky, wall-adapted LES (WALE), the variational multi-scale, and detached-eddy simulation (DES) models. Details on the models and their implementation in Hydra-TH are given in the Hydra-TH theory manual [4]. The discussion of the models is beyond the scope of this paper, more details for the Spalart-Allmaras, k - ϵ , DES , and WALE models can be found in [21, 18, 22, 19], respectively.

While RANS models directly compute statistics, LES produces one realization of a space-, and time-dependent (fluctuating) flow field. If the flow becomes statistically stationary in LES, the temporal variations of the fields can be assumed to be different realizations and can be used to estimate statistics. Hydra-TH can calculate various run-time statistics, including mean velocity, mean pressure, mean temperature, mean heat flux, mean wall shear stress, root-mean-square (RMS) pressure, RMS temperature, turbulent kinetic energy, Reynolds stress tensor, etc. The full list of available statistics is documented in the Hydra-TH User Manual [3].

In statistically stationary flows, the mean (i.e., first moment) of an instantaneous variable ϕ is computed by Δt -weighted time-averages over N time steps:

$$\langle \phi \rangle \approx \frac{\sum_{i=1}^N \phi^i \Delta t^i}{\sum_{i=1}^N \Delta t^i} \quad (58)$$

where i is the time step. The variance (i.e., second moment or square of the RMS) of ϕ is computed by

$$\langle \phi'^2 \rangle = \langle (\phi - \langle \phi \rangle)^2 \rangle \quad (59)$$

Run-time estimation of turbulence statistics can take a significant portion of simulation time. This is especially the case if many different statistics are computed and/or the algorithm is general enough to accommodate different types of statistics. The implementation in Hydra-TH has been designed with the following requirements in mind:

1. *The computation of statistics is a small fraction of the total simulation time.* Only the variables required to compute the given moment are accumulated. Statistics required by two (or more) moments are only accumulated once. An example is if the user requests the pressure variance, $\langle p'^2 \rangle = \langle (p - \langle p \rangle)^2 \rangle$, and the pressure-velocity covariance, $\langle p' \mathbf{v}' \rangle = \langle (p - \langle p \rangle)(\mathbf{v} - \langle \mathbf{v} \rangle) \rangle$, the mean, $\langle p \rangle$, is only accumulated once.
2. *General.* The user may request statistics in cells, nodes, and on surfaces, regardless of an instantaneous variable's internal representation. The implementation handles both ordinary and central moments, and general correlations of arbitrary number of scalars $\langle a' b' \dots z' \rangle$, vectors $\langle a'_i b'_i \dots w'_i z'_i \rangle$, and second-order tensors $\langle a'_{ij} b'_{ij} \dots z'_{ij} \rangle$. (Here summation on repeated indices is not implied.)

3. *Easily extensible with new statistics.* Higher-order moments (such as skewness, kurtosis, etc.), correlations of an arbitrary number of any combination of primitive variables can be easily added.

Some statistics, such as turbulent kinetic energy spectra and force power spectral densities, are more sensible to obtain from post-processing time-history output as opposed to extracting them at run-time. For example, Fourier transforms of the fluctuating fields can be obtained based on instantaneous time-history output that is also readily available in Hydra-TH.

In summary, Hydra-TH has various options for directly computing the mean fields in a turbulent flow using RANS models, or via LES where time-averaged run-time statistics can be collected in statistically stationary flows.

4 MULTIPHASE FLOW MODELING STRATEGY

For multi-phase flow problems Hydra-TH solves ensemble-averaged governing equations [8]. The ensemble-average of a scalar variable, Φ , is defined by

$$\bar{\Phi}(\mathbf{x}, t) = \int_{\mu} \Phi f(\mathbf{x}, t; \Phi) d\Phi(\mu) \quad (60)$$

where $f(\mathbf{x}, t; \Phi)$ is the probability density function defined over all realizations (μ) of Φ . Using the *component indicator* or *characteristic function* [8],

$$\mathcal{X}_k(\mathbf{x}, t; \mu) = \begin{cases} 1 & \text{if } \mathbf{x} \in k \text{ in realization } \mu \\ 0 & \text{otherwise} \end{cases} \quad (61)$$

ensemble averages of various physical quantities are defined as

$$\begin{aligned} \text{Volume fraction:} \quad \alpha_k &= \overline{\mathcal{X}_k} \\ \text{Phasic density:} \quad \bar{\rho}_k &= \frac{\overline{\mathcal{X}_k \rho}}{\alpha_k} \\ \text{Phasic velocity:} \quad \tilde{\mathbf{v}}_k &= \frac{\overline{\mathcal{X}_k \rho \mathbf{v}}}{\alpha_k \bar{\rho}_k} \\ \text{Phasic specific internal energy:} \quad \tilde{u}_k &= \frac{\overline{\mathcal{X}_k \rho u}}{\alpha_k \bar{\rho}_k} \\ \text{Phasic fluctuation (Reynolds) kinetic energy:} \quad \tilde{\kappa}_k &= \frac{\overline{\mathcal{X}_k \rho |\mathbf{v}'_k|^2}}{2\alpha_k \bar{\rho}_k}, \quad \mathbf{v}'_k = \mathbf{v} - \tilde{\mathbf{v}}_k \\ \text{Phasic total energy:} \quad \tilde{e}_k &= \tilde{u}_k + \frac{|\tilde{\mathbf{v}}_k|^2}{2} + \tilde{\kappa}_k \end{aligned} \quad (62)$$

where tilde indicates mass-weighted (i.e., Favre) averaging. Without derivation, the equations governing the ensemble average of mass, momentum, and total energy for all phases

$k = 0, \dots, K-1$ are

Conservation of mass:

$$\frac{\partial}{\partial t} \underbrace{(\alpha_k \bar{\rho}_k)}_{\overline{\mathcal{X}_k \rho}} + \nabla \cdot \underbrace{(\alpha_k \bar{\rho}_k \tilde{\mathbf{v}}_k)}_{\overline{\mathcal{X}_k \rho \mathbf{v}}} = \underbrace{\overline{\Gamma_k}}_{\overline{\rho(\mathbf{v}-\mathbf{v}_i) \cdot \nabla \mathcal{X}_k}} \quad (63)$$

Interfacial mass transfer

Conservation of momentum:

$$\frac{\partial}{\partial t} \underbrace{(\alpha_k \bar{\rho}_k \tilde{\mathbf{v}}_k)}_{\overline{\mathcal{X}_k \rho \mathbf{v}}} + \nabla \cdot \left(\underbrace{\alpha_k \left[\bar{\rho}_k \tilde{\mathbf{v}}_k \otimes \tilde{\mathbf{v}}_k - \mathbf{T}_k^{Re} \right]}_{\overline{\mathcal{X}_k \rho \mathbf{v} \otimes \mathbf{v}}} + \underbrace{\alpha_k \left(\bar{p}_k \mathbf{I} - \bar{\boldsymbol{\tau}}_k \right)}_{-\overline{\mathcal{X}_k \mathbf{T}}} \right) =$$

$$\underbrace{\alpha_k \bar{\rho}_k \tilde{\mathbf{b}}_k}_{\overline{\mathcal{X}_k \rho \mathbf{b}}} + \underbrace{\overline{\mathbf{v}_{ki}^m \Gamma_k}}_{\overline{\rho \mathbf{v}(\mathbf{v}-\mathbf{v}_i) \cdot \nabla \mathcal{X}_k}} + \underbrace{\left(\overline{p_{ki}} - \overline{\tau_{ki}} \right) \nabla \alpha_k + \overline{\mathbf{M}'_k}}_{\overline{\mathbf{M}_k \equiv -\mathbf{T} \cdot \nabla \mathcal{X}_k}}$$

Interfacial momentum due to mass transfer Interfacial force

Conservation of total energy:

$$\frac{\partial}{\partial t} \underbrace{(\alpha_k \bar{\rho}_k \tilde{e}_k)}_{\overline{\mathcal{X}_k \rho(u + \frac{1}{2}|\mathbf{v}|^2)}} + \nabla \cdot \left(\underbrace{\alpha_k \left[\bar{\rho}_k \tilde{e}_k \tilde{\mathbf{v}}_k - \mathbf{T}_k^{Re} \right]}_{\overline{\mathcal{X}_k \rho(u + \frac{1}{2}|\mathbf{v}|^2) \mathbf{v}}} + \underbrace{\alpha_k \left[\bar{p}_k \mathbf{I} - \bar{\boldsymbol{\tau}}_k \right]}_{-\overline{\mathcal{X}_k \mathbf{T} \cdot \mathbf{v}}} \cdot \tilde{\mathbf{v}}_k \right) =$$

$$-\nabla \cdot \underbrace{\left(\alpha_k \left[\tilde{\mathbf{q}}_k + \mathbf{q}_k^{Re} \right] \right)}_{\overline{\mathcal{X}_k \mathbf{q}}} + \underbrace{\alpha_k \bar{\rho}_k \left(\tilde{\mathbf{r}}_k + \tilde{\mathbf{b}}_k \right) \cdot \tilde{\mathbf{v}}_k}_{\overline{\mathcal{X}_k \rho \mathbf{b} \cdot \mathbf{v} + \mathcal{X}_k \rho r}} + \underbrace{\overline{E_k}}_{\overline{\mathbf{q} \cdot \nabla \mathcal{X}_k}}$$

Interfacial heat source

$$+ \underbrace{\overline{\Gamma_k \left(u_{ki} + \frac{\left(\overline{v_{ki}^e} \right)^2}{2} \right)}}_{\overline{\rho(u + \frac{1}{2}|\mathbf{v}|^2)(\mathbf{v}-\mathbf{v}_i) \cdot \nabla \mathcal{X}_k}} + \underbrace{\overline{W'_k} + \left[\left(\overline{p_{ki}} - \overline{\tau_{ki}} \right) \nabla \alpha_k + \overline{\mathbf{M}'_k} \right] \cdot \tilde{\mathbf{v}}_k}_{\overline{W_k \equiv -\mathbf{T} \cdot \mathbf{v} \cdot \nabla \mathcal{X}_k}}$$

Interfacial energy due to mass transfer Interfacial work

The terms in boxes are a result of the averaging, and as the mean contains no information on higher moments, see Eq. (60), closure approximations are required. The averaged pressures are given by equations of state in terms of averaged phasic quantities:

$$\bar{p}_k = \mathcal{EOS}(\bar{\rho}_k, \tilde{u}_k) \quad (66)$$

where \tilde{u}_k is the internal energy of phase k . Augmenting Eqs. (63–66) with the *compatibility equation*

$$\sum_k \alpha_k = 1 \quad (67)$$

yields a closed system governing inter-penetrating continua – provided the effects of the boxed approximations are specified, see [8, 16] for details. Eqs. (63–65) represent compressible media in mechanical and thermal non-equilibrium and pressure equilibrium. Pressure difference between phases can be accounted for by adding bulk-pressure-difference models. If virtual mass and interfacial pressure terms are incorporated into Eqs. (63–65), the mathematical problem becomes well-posed in the inviscid limit, see [7, 23] for details of hyperbolization.

Figure 3 shows three different solution strategies being implemented in Hydra-TH. At this time, “Option 1” is implemented and discussed in §2, the implementations of “Options 2 and 3” are currently underway. Figure 4 shows a snapshot of a “proof-of-concept” calculation using Option 1. Two fields, α_1, α_2 , are simulated in a vortex street of a circular cylinder using a semi-implicit projection algorithm in which the fields are coupled only via the single pressure. Initially $\alpha_1 = 0, \alpha_2 = 1$, and a mass of $\alpha_1 = 0.1$ is injected at the cylinder wall into the carrier fluid. It is interesting to note that the extreme cases of $\alpha_k = 0$ and 1, i.e. phase appearance and disappearance, are properly handled by the algorithm, without requiring any special treatment used in most commercial multi-phase flow algorithms.

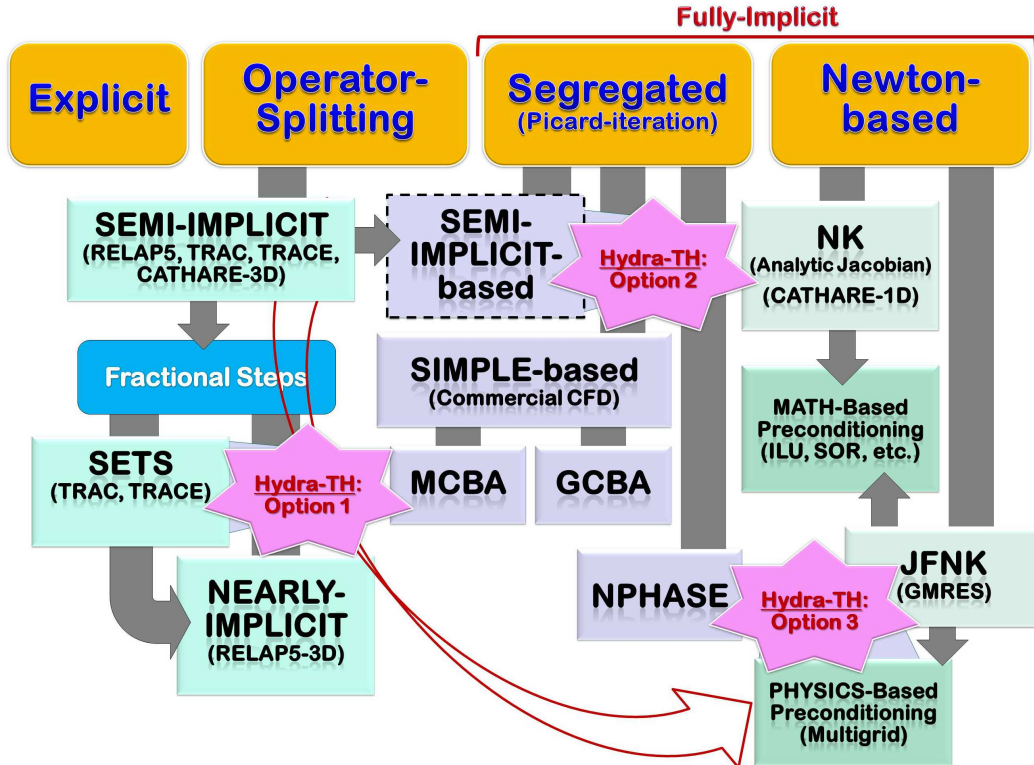
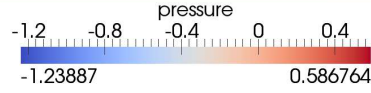
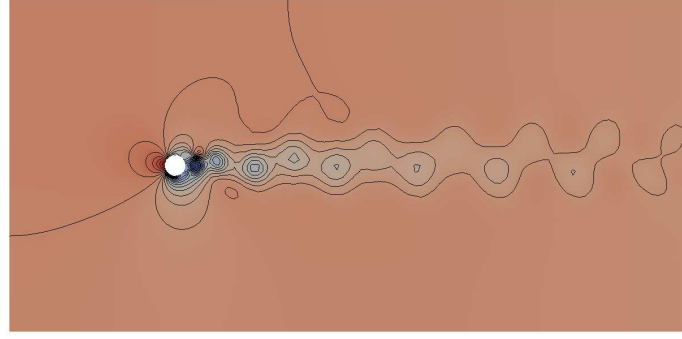
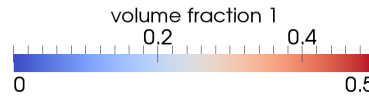
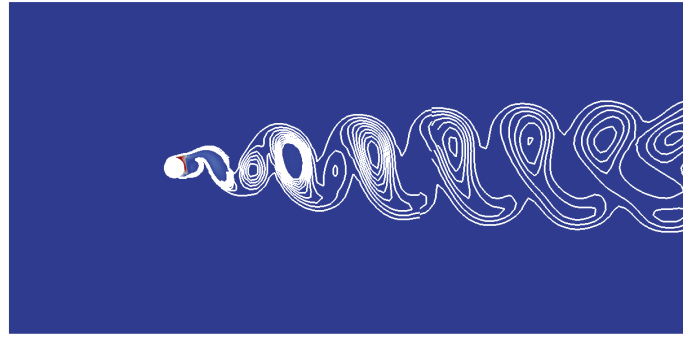


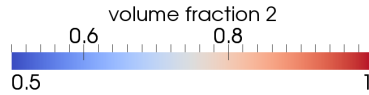
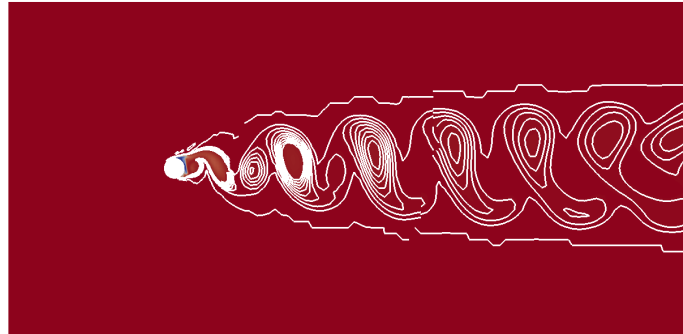
Fig. 3: Multi-fluid modeling in Hydra-TH.



(a) Pressure.



(b) Volume fraction 1. The color legend is scaled to the extremes, while the contour lines divide the range 0.001-0.01 into 10 equal portions.



(c) Volume fraction 2. The color legend is scaled to the extremes, while the contour lines divide the range 0.99-1.0 into 10 equal portions.

Fig. 4: Proof-of-concept demonstration of the “Option 1” (see Figure 3) multi-field solver in Hydra-TH using vortex shedding with two fields of equal densities. The volume fraction initial conditions are $\alpha_1 = 0$ and $\alpha_2 = 1$. An influx of $\alpha_1 = 0.1$ is prescribed at the cylinder surface and advected downstream, from left to right.

5 VALIDATION & VERIFICATION STRATEGY

Verification and validation provides confidence in design, implementation and output of scientific simulation software. The Hydra code team recognizes that active test development and frequent testing are critical to the success of any code project. For Hydra-TH, regression testing is the primary testing method where three test suites organize the tests by resource requirements. Short running tests are separated from the longer tests, and these short tests are also categorized into serial and parallel tests. Each suite runs nightly on Ubuntu Linux and Mac OSX platforms. Results are posted on a website dashboard. The website also documents test statistics for individual tests and maintains a historical record of the test suite. Developers are required to execute the quick running serial and parallel suites on at least two platforms before committing code changes. There is a zero-tolerance policy for pre-commit regression testing that is strictly adhered to for Hydra development.

A typical example of a verification test problem is presented here. This example consists of a suite of five lid-driven skewed cavity problems based on the work by Erturk and Dursun [10], with $\alpha = 15, 30, 45, 60, 90^\circ$. Each skewed cavity uses three grids with 32×32 , 128×128 and 256×256 elements. Note that the results by Ghia, et al. [11] are also available for the specific 90° lid-driven cavity, but a direct comparison with this data is not included.

The geometrical configuration for the lid-driven cavity is shown in Figure 5 with α defining the skew angle. On the bottom and side walls, no-slip/no-penetration boundary conditions were prescribed. Along the top “lid”, a no-penetration boundary condition along with a unit lid velocity are prescribed. A single nodal pressure was prescribed in the bottom right-hand corner to set the hydrostatic pressure level.

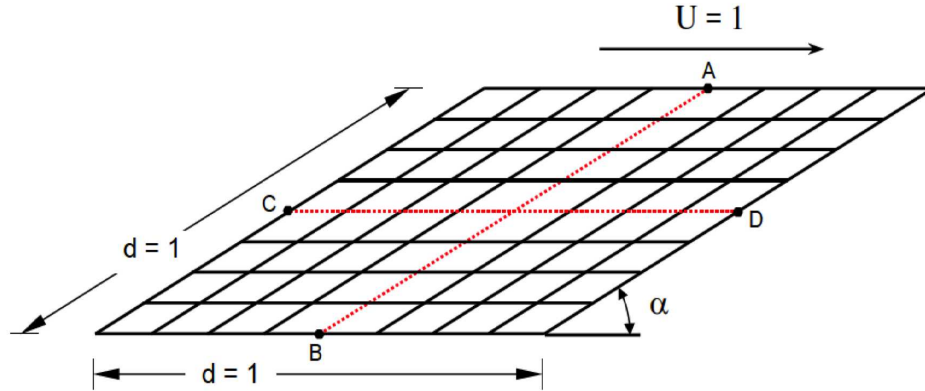


Fig. 5: Skewed lid-driven cavity geometry (reproduced from Erturk and Dursun[10] without permission).

For all computations, $CFL_{\max} = 10$ and backward-Euler time integration is used since the goal is a steady-state solution. Time history plots of the global kinetic energy indicate that a steady-state solution is reached by ≈ 10 time units. Note that the diffusional time-scale varies with each skew angle slightly with larger time-scales required for the larger skew angles. All problems for this example are run for 40 time units. Velocity data is extracted along the red center lines shown in Figure 5 for direct comparison with the reference data provided by Erturk and Dursun. The x-velocity profile is plotted against the vertical centerline, and the y-velocity profile is plotted against the horizontal centerline as shown in Figures 6.

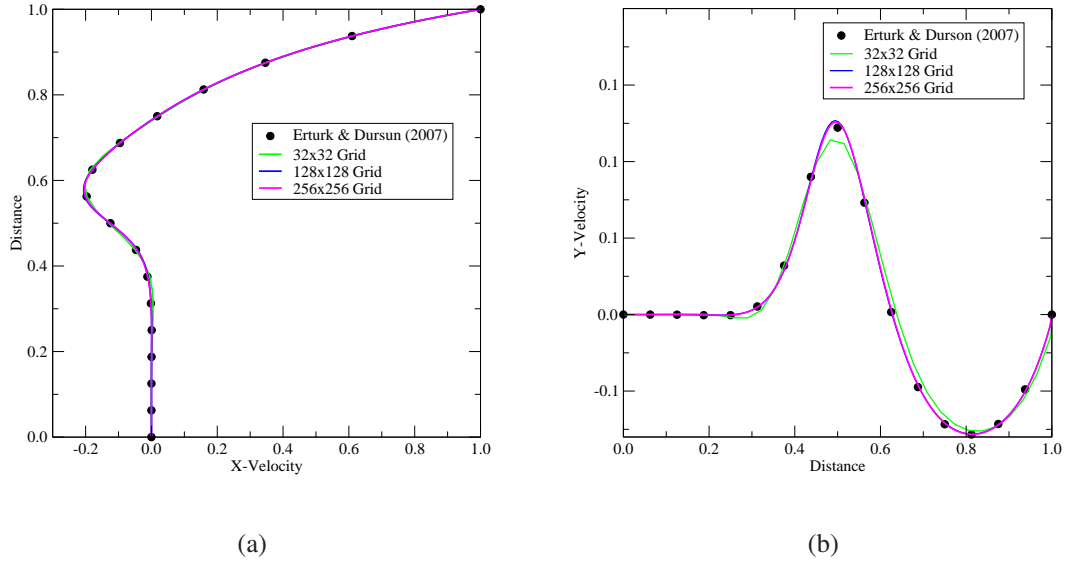


Fig. 6: 15° lid-driven cavity: (a) x-velocity, (b) y-velocity.

All of the lid-driven cavity problems achieve a steady-state (as verified by the global kinetic energy and velocity time-histories), and this provides a convenient way to assess the convergence behavior as the mesh is refined. All of the cavity meshes used uniform meshing, albeit with severely skewed elements for the 15° cavity. Table 1 shows the asymptotic behavior of the kinetic energy (quadratic velocity) as a function of the x-mesh size (h) which indicates $O(h^2)$ convergence in all velocity components for all of the skew angles.

Cavity Angle	Global Kinetic Energy Correlation
15°	$0.00020907 - 0.006877 h^2$
30°	$0.00038731 - 0.010046 h^2$
45°	$0.00053854 - 0.014590 h^2$
60°	$0.00067314 - 0.019690 h^2$
90°	$0.00086136 - 0.029630 h^2$

Table 1: Convergence behavior of the global kinetic energy vs. h for the lid-driven skewed cavities.

We recognize the need for continued and comprehensive verification and validation testing as Hydra-TH matures. We are currently organizing many of these regression tests into validation and verification classes. Each test is classified as a verification or validation and is documented in a concise report, which includes a problem description, appropriate figures and references. Results are emphasized with comparison metric definitions and either the complete description or references to all the required input files to reproduce the results. Each report is included in a master document that will be the official V&V report for Hydra-TH. We anticipate approximately 20 such tests in this document by the end of 2013.

6 EXAMPLE APPLICATION: GRID-TO-ROD FRETTING

Within the core of a pressurized-water nuclear reactor, water flow is used to cool the irradiated fuel rods. Grid-to-rod fretting in such reactors is a flow-induced vibration problem that results in wear and failure of the rods. GTRF wear is one of the leading causes for leaking nuclear fuel and costs power utilities millions of dollars in preventive measures. In order to understand the root causes of such fuel leaks, we investigate the complex turbulent coolant flow around fuel-rod bundles. Our ultimate goal is to accurately predict the turbulent excitation forces on the fuel rods, along with the coupled structural response of the rods and their supports. To date, it has not been possible to completely characterize the flow-induced fluid-structure interaction (FSI) problem for GTRF. Indeed, given the incompressible nature of the coolant, the relatively high Reynolds number, and the flexible character of the fuel rods and spacers, the FSI problem at the reactor core scale is daunting.

This section discusses the use of LES (see §3) in Hydra-TH for computing the GTRF problem. The second-order semi-implicit incremental projection method, discussed in §2.3, is used to solve the single-phase incompressible Navier-Stokes equations governing an isothermal flow. The calculations use hybrid meshes, containing different cell types, generated with Hexpress/Hybrid, a.k.a. Spider,³ for a 3×3 (§6.1) and a 5×5 (§6.2) rod-bundle sub-assembly, respectively. Our earlier study [5], provides details on calculations using LES, DES, and the Spalart-Allmaras turbulence models using meshes generated by Cubit.

6.1 LES on a 3×3 Rod-Bundle Sub-Assembly

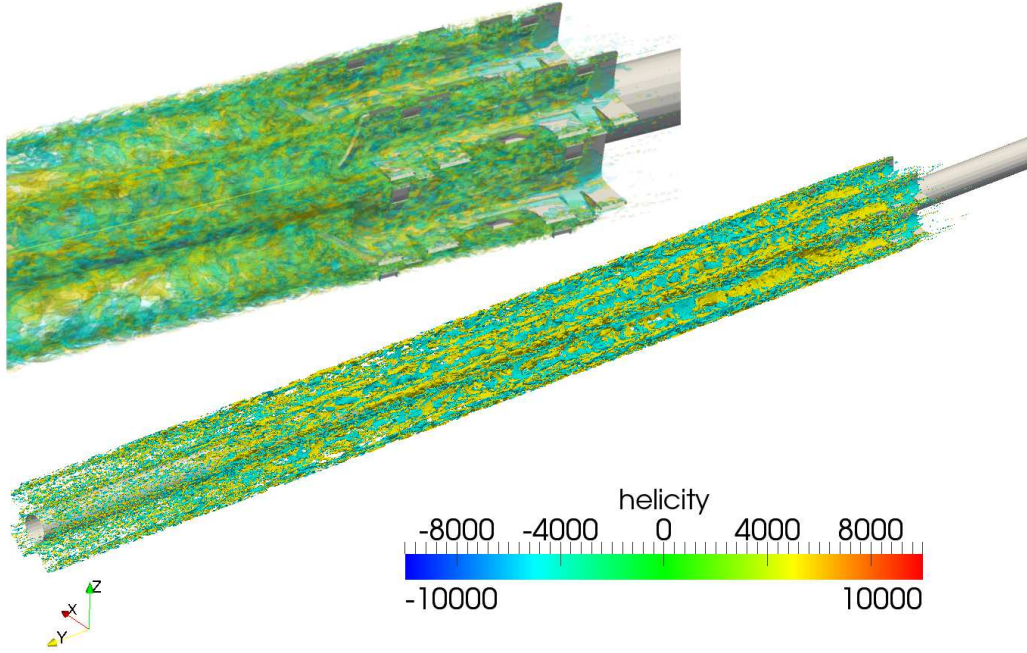
A qualitative picture of the instantaneous flow behind the mixing vanes is shown in Figure 7 with isosurfaces of the helicity. The vortices generated by the spacer and the mixing vanes are advected downstream. Figure 7 shows that the neutrally dissipative advection algorithm in Hydra-TH does an excellent job in maintaining the complex vortex structures far downstream, i.e., introduces minimal phase errors.

Similar to our earlier LES calculations on the 3×3 rod-bundle [5], a series of preliminary coarse-mesh simulations were conducted using the Spider meshes to determine when a statistically stationary flow is achieved. The time-evolution of the domain-average kinetic energy (not shown) was used as an indicator, based on which the time of approximately 0.1s was chosen as the starting point for collecting time-averaged flow statistics until the end of the simulation at $t = 1.0$ s.

Six calculations, using Spider meshes with approximately 2 million (M), 7M, 14M, 27M, 30M, and 47M cells have been carried out.

The instantaneous pressure is plotted in Figure 8 for different meshes. The end-point coordinates of the lines along which the pressure line plots have been obtained are $(3.3588\text{E-}3, -9.6520\text{E-}2, 3.3588\text{E-}3)$ and $(3.3588\text{E-}3, 3.0480\text{E-}1, 0.33588\text{E-}3)$. For more detail on the flow geometry see [5]. The vertical lines in Figure 8 delineate the bounds of the spacer and the mixing vanes. It is reassuring that the pressure lines are qualitatively very similar for all mesh resolutions. Since the hydrostatic pressure at the outflow is fixed at $p = 0$, the value of the calculated inlet pressure determines the pressure drop over the whole domain. The pressure drop for the 47M Spider mesh is 11.425 kPa, however, this value does not seem to have converged for this series of calculations. In contrast to the

³<http://www.numeca.be/index.php?id=hexhyb>



(a) Instantaneous helicity isosurfaces for the 47M Spider mesh.

Fig. 7: Instantaneous snapshots of helicity ($\mathbf{v} \cdot \boldsymbol{\omega}$) isosurfaces for the 2M and 47M Spider meshes.

pressure observed with the Cubit meshes [5], the pressure drop is monotonically increasing with mesh resolution.

The mean pressure along the rod is also plotted in Figure 8. A large drop in the mean pressure through the spacer indicates that most of the pressure loss is due to the spacer. In spite of the turbulent flow induced by the spacer, the characteristic peaks and troughs in the profile of the mean pressure are very much reproducible throughout the spacer using the 2M, 7M, and 14M meshes. Downstream of the mixing vanes a slight wave in the mean pressure is apparent in the coarsest 2M-mesh simulation. The mean pressure using the 7M mesh appears as what one would intuitively expect for a turbulent pipe flow: from approximately $y = 0.175m$, the mean pressure linearly decreases to zero.

The RMS pressure along the rod is plotted in Figure 9(a) for the two coarsest Spider meshes. The fluctuating pressure force is probably the most important quantity to compute accurately for a reasonable representation of the forces acting on the fuel rods. The figure shows that the RMS pressure peaks at the downstream end of the spacer for the 7M and 14M meshes. This is expected, since this is where the level of turbulent kinetic energy is the largest. While the downstream locations of the peaks are somewhat aligned for the varying meshes, their amplitudes and downstream evolution are quite different. The 2M mesh is too coarse to adequately capture the second pressure moment. At this point we are not in a position to draw any conclusions regarding the grid-convergence of the RMS pressure. Regardless, the turbulent kinetic energy (and the RMS pressure) must decay downstream as no energy production occurs downstream of the mixing vanes.

The total force and its two components, the pressure and viscous forces, have been extracted in time on the central rod and the spacer. Surface forces are computed by inte-

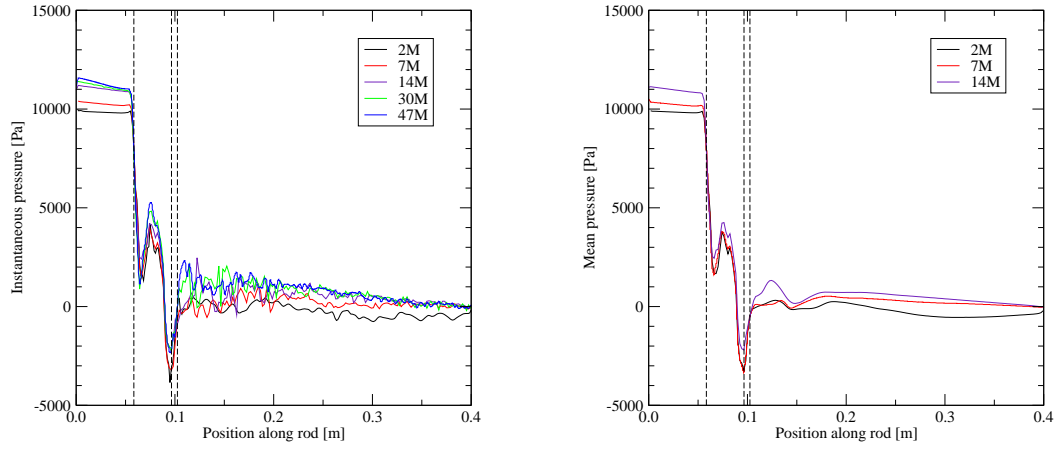
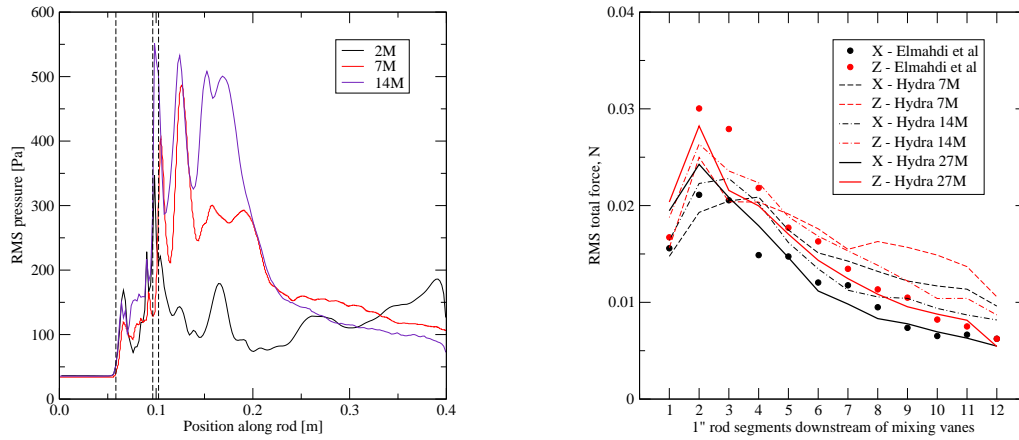
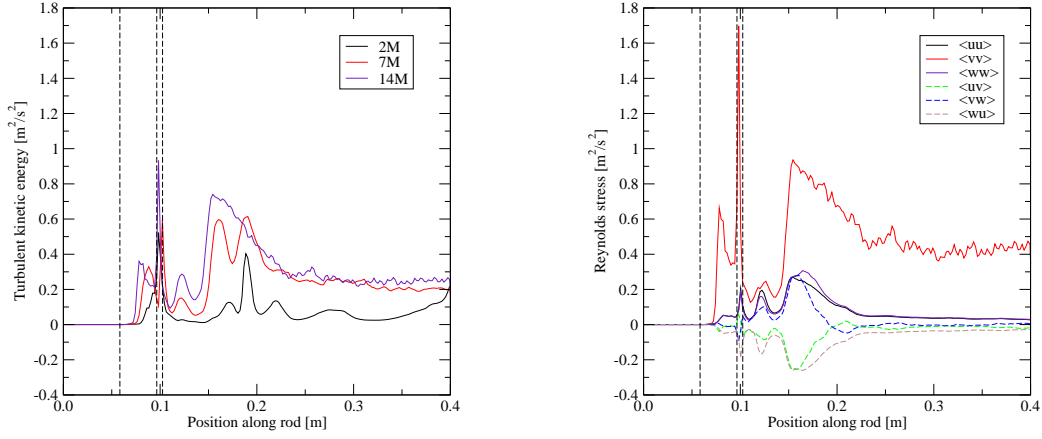


Fig. 8: Instantaneous (left) and mean (right) pressure line plots for different meshes.



(a) RMS pressure integrated over the full length of the central rod for three different meshes. (b) RMS total force on the central rod integrated in 1-inch segments downstream of the mixing vanes. The Star-CCM+ results are from the LES calculations in [9].

Fig. 9: Second moments of the pressure (integrated for the full length) and the total force (dominated by the pressure force) in segments.



(a) Turbulent kinetic energy along the rod for three different meshes. (b) Reynolds stress along the rod for the 14M mesh.

Fig. 10: Second moments of the fluctuating velocity field for three different meshes.

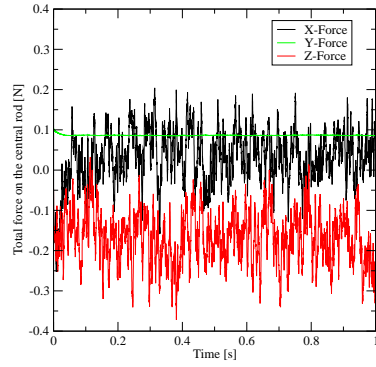
grating pressure and shear stress over the given surface:

$$F_i(t) = - \int p(t) n_i dA + 2 \int \mu S_{ij}(t) n_j dA, \quad (68)$$

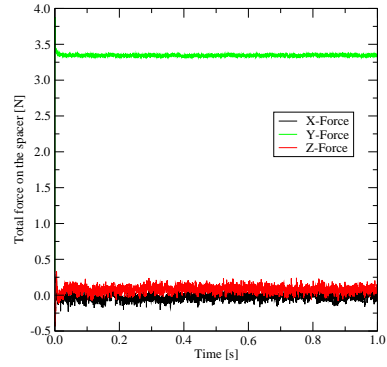
where \mathbf{F} , p , \mathbf{n} , A , and $S_{ij} = (v_{i,j} + v_{j,i})/2$ denote the total force, pressure, outward surface normal, surface area, and the strain rate of the instantaneous velocity, \mathbf{v} , respectively. This gives the force time history that can be used to compute power spectral distributions or fed directly into structural dynamics codes to compute wear. The total, pressure, and viscous force time-histories for the 7M case are presented in Figure 11, which shows that the mean forces are similar to those computed using the Cubit meshes presented in [5]. On the other hand the pressure force acting on the central rod, probably the most important quantity for the GTRF problem, shows much larger fluctuations about the mean for the Spider mesh relative to the Cubit results.

The total forces have also been integrated in 12 one-inch segments downstream of the mixing vanes. This gives details on the spatial distribution of the forces loading the central rod and allows for a more direct comparison with the Star-CCM+ LES results by Elmahdi, et al. [9]. In Figure 9(b) the RMS total force is given in segments for the 7M, 14M, and 27M Spider meshes, compared to that of the Star-CCM+ LES using a 47M-cell mesh. The RMS forces extracted from the 2M simulation are inadequate to provide meaningful second moments of the force loading the rod and are not shown. The RMS forces computed by Hydra-TH using the 7M, 14M, and 27M meshes are quite close and gradually approach those of Star-CCM+, even with significantly coarser meshes.

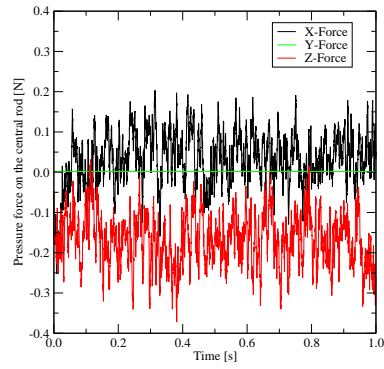
Additional insight into the fluctuating velocity field is found by examining the turbulent kinetic energy and Reynolds stresses shown in Figure 10. In Figure 10(a) the downstream spatial evolution of the turbulent kinetic energy (TKE) is plotted for the 2M, 7M, and 14M meshes. Similar to the pressure variance in Figure 9, the TKE, $k = \langle \mathbf{v}' \cdot \mathbf{v}' \rangle / 2$, peaks in the vicinity of the mixing vanes and stays at a relatively high value until approximately 0.2m downstream. This reinforces our earlier observation that the highest level of



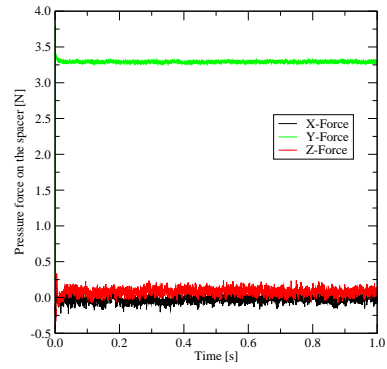
(a) Total force on the central rod.



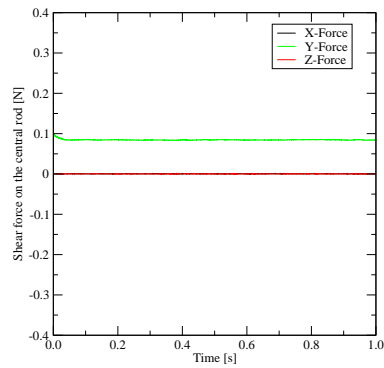
(b) Total force on the spacer.



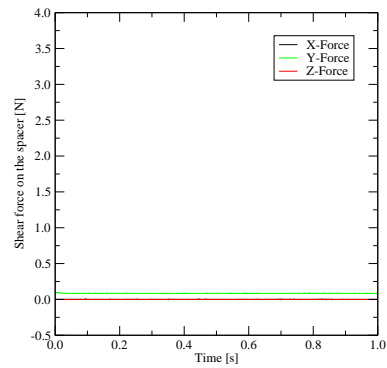
(c) Pressure force on the central rod.



(d) Pressure force on the spacer.



(e) Shear force on the central rod.



(f) Shear force on the spacer.

Fig. 11: Total, pressure, and shear force time histories on the central rod and spacer for the 7M Spider mesh.

TKE occurs close to the downstream edge of mixing vanes. Figure 10(a) also indicates that the 2M-cell mesh is too coarse to produce a qualitatively correct TKE evolution; similar to the RMS pressure, the TKE should also decay downstream.

Figure 10(b) depicts the downstream evolution of the different components of the Reynolds stress tensor, $\langle \mathbf{v}'\mathbf{v}' \rangle$ for the 14M mesh. The figure shows that the flow downstream of the mixing vanes remains highly anisotropic until the end of the computational domain: almost all kinetic energy is in the streamwise component, $\langle v'v' \rangle$, of the velocity, $\mathbf{v} = (u, v, w)$, i.e., the streamwise fluctuations are large compared that of both cross-stream components, $\langle u'u' \rangle$, $\langle w'w' \rangle$, in x and z directions, respectively.

6.2 LES on a 5×5 Rod-Bundle Sub-Assembly

This section discusses the calculations for the 5×5 fuel-rod bundle. The geometry was provided in CAD format by Westinghouse, and corresponds to the experimental configuration used at Texas A&M, where particle image velocimetry (PIV) measurements were carried out. The flow domain is shown in Figure 12. Not shown here are the exterior walls of the flow housing used in the experimental facility. Additional details on the experimental configuration and results may be found in Conner, et al. [6] and [28].

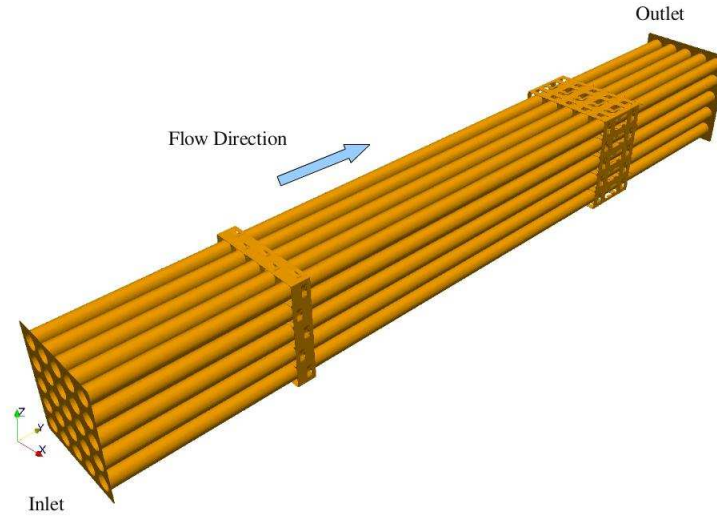


Fig. 12: Flow domain for the 5×5 rod bundle showing the rods, the inlet/outlet planes, the support, and the spacer grid.

At the inlet of the flow domain, a constant prescribed velocity $(0.0, 2.48, 0.0)\text{m/s}$ is applied with the fluid properties for water at 24°C and atmospheric pressure. This corresponds to a Reynolds number of approximately 28,000 based on the hydraulic diameter for the rod bundle. At the surfaces of the flow housing, rods, support and spacer grids, no-slip/no-penetration velocity conditions were prescribed. Homogeneous Neumann conditions for velocity along with a zero-pressure condition were prescribed at the outflow plane. A fixed $CFL = 4$ condition was used with automatic time-step control for all computations.

Following the procedures to perform LES calculations on the 3×3 rod-bundle,

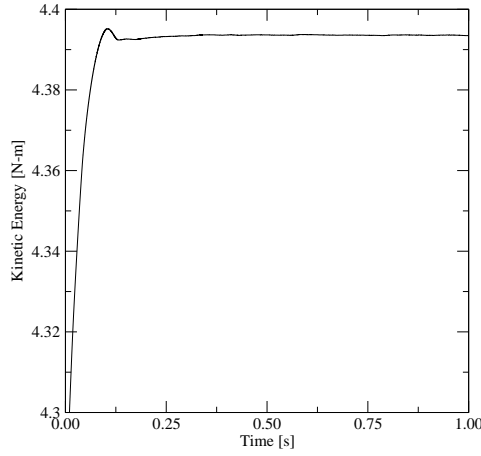


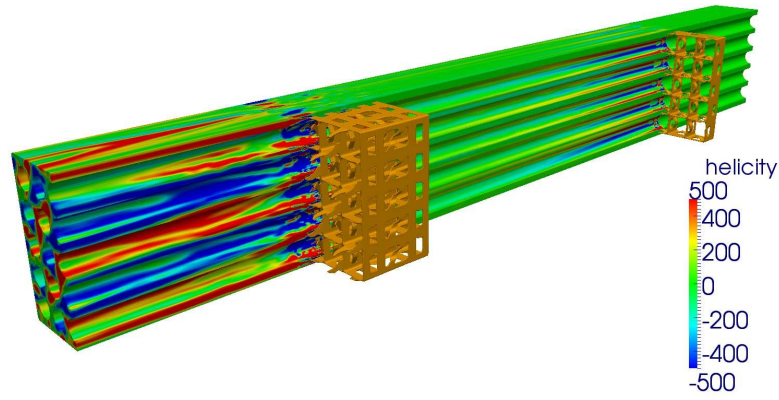
Fig. 13: Domain-average kinetic energy, $\int \rho \mathbf{v} \cdot \mathbf{v} / 2 d\Omega$, vs. time for the 14M 5×5 rod bundle.

Point	(x, z) Position [$10^{-3}m$]
A	(-6.3, 6.3)
B	(-6.3, 0.0)
C	(-6.3, -6.3)
D	(0.0, -6.3)
E	(6.3, -6.3)
F	(6.3, 0.0)
G	(6.3, 6.3)
H	(0.0, 6.3)

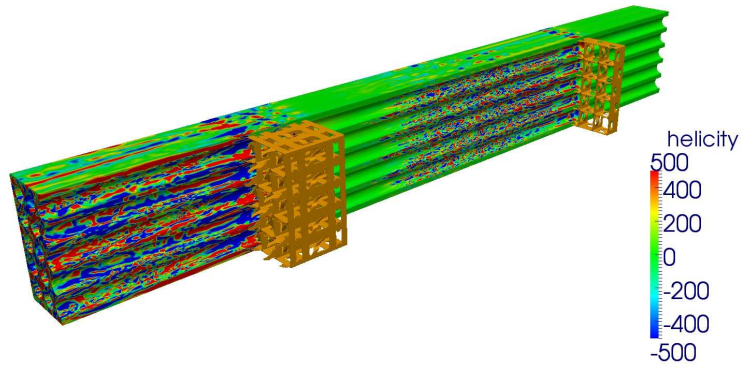
Table 2: Sample points A – H used to extract line-data for comparison with experimental data.

outlined in [5], a series of preliminary coarse-mesh calculations were conducted to determine when a stationary turbulent state would be achieved and to test the sensitivity to mesh resolution and the time-step size. Figure 13 shows the global, i.e. domain-average, kinetic energy, $\int \rho \mathbf{v} \cdot \mathbf{v} / 2 d\Omega$, as a function of time. Here Ω denotes the volume of the flow domain. Based on these preliminary calculations, a time of approximately 0.2s was chosen as the starting point for collecting time-averaged flow statistics until the end of the simulation at $t = 1.0s$.

In order to illustrate the impact of increasing mesh resolution on the flow, Figure 14 shows snapshots of the instantaneous helicity field for the 5×5 rod bundle for two different mesh resolutions. For the 14M mesh, there are relatively large coherent structures downstream of the support and spacer grid. In contrast, the flow structures captured by the 96M mesh are significantly smaller and appear more randomly distributed spatially. In both cases, the influence of the mixing vanes on the spacer grid is apparent. In order to compare to the experimental data, discussed in [28], a series of line plots were extracted from the mean velocity field for the 14M-mesh 5×5 run at locations that fall in the planes of the PIV measurements. All line data were measured relative to the so-called “weld-nugget” located on the spacer grid. The “weld nugget” is located at 38.1 mm from the bottom of the spacer grid [27] as shown in Figure 15(a). The line-data extracted from the computation

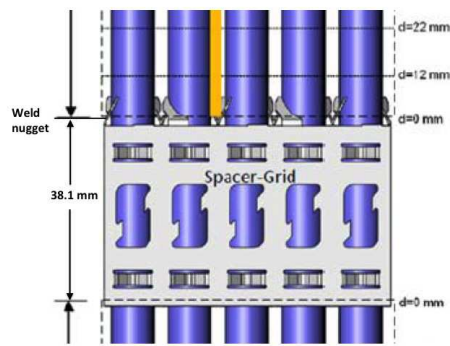


(a) 14M Mesh.

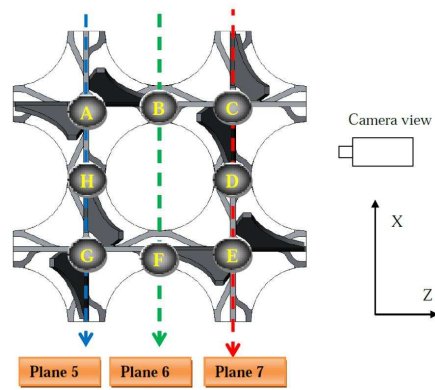


(b) 96M Mesh.

Fig. 14: Snapshots of the instantaneous helicity field for the 14M and 96M element meshes.



(a) Weld nugget location.



(b) Sample points.

Fig. 15: Locations relative to the “weld nugget” used for extracting data along planes 5, 6 and 7. (Reproduced from [28]) without permission.)

was located at the positions indicated in Figure 15. The coordinates of the sample points A – H are shown in Table 2 and are relative to the center of rod 13 in Figure 3 in [28]. In the flow direction, the line-data is extracted for $0.05 \leq y \leq 0.09$ m corresponding to the region where PIV data is available in the region downstream of the spacer grid. Following Yan, et al. [28], mean velocities are compared at points A, C, D, E, G, and H as shown in Figure 16. Here, the streamwise velocity in the experiments corresponds to the y -velocity in the computation, while the lateral velocity corresponds to the x -velocity. Yan, et al. [28], estimated the systematic uncertainty in the velocities due to the PIV measurements, software acquisition, etc, to be a maximum of 0.199m/s. The statistical uncertainty, which is a function of the number of snapshots of the velocity, is estimated to be $\pm 0.167V_{\text{inlet}}$ in the lateral direction, and $\pm 0.15V_{\text{inlet}}$ in the axial direction, where $V_{\text{inlet}} = 2.48\text{m/s}$. All experimental data has been plotted with the uncertainty bounds provided by Dominguez-Ontiveros and Hassan, see also [6].

The line plots of velocity for the 96M mesh are presented in Figure 16 for stations A – H. The 96M results match the experimental data more closely at all points A – H. However, the stream-wise velocity still appears to be slightly over-predicted. In contrast, the x -velocities fall within the uncertainty bounds for points A, C, E, and G, while the x -velocities at points D and H have similar profiles but are not quite within the uncertainty bounds. Overall, the 96M results compare very well to the experimental data.

Time-averaged velocities in plane-5, see Figure 15, from [6] are shown in Figure 17 with the computed time-averaged mean velocity fields. Similarly, the experimental and computed mean velocity fields on plane-7 are shown in Figure 18. The data in the figures have been scaled relative to the 2.48m/s inlet velocity. The peak velocities in the axial direction are slightly under-predicted in the Hydra-TH computations, while the lateral velocities are slightly over-predicted. This is likely due to the very coarse mesh used in this LES calculation. While the peak velocities appear to be relatively close to those found experimentally, inspection of Figures 17 and 18 indicates that the deflection in the velocity vectors due to the mixing vanes and the flow housing is well-captured by the simulation.

7 CONCLUSION

We gave an overview of Hydra-TH, a code being developed at Los Alamos for simulation of thermal-hydraulics phenomena in nuclear reactor applications. We also described some algorithmic details of a new fully-implicit projection algorithm being implemented for both single and multi-phase flows with phase change. Some recent results from a series of isothermal single-phase turbulent flow calculations of the grid-to-rod-fretting (GTRF) problem have also been reported. Progress towards a simulation capability for advanced thermal-hydraulics may be summarized as follows:

1. *Fully-implicit projection algorithm.* A new fully-implicit solution algorithm has been described that is based on existing explicit and semi-implicit incremental projection for incompressible flows. The algorithm is targeted for efficient and robust simulation of slow transients, enabling time steps sizes well above the stability limits of traditional semi-implicit algorithms. As a consequence, the long-time-integrated effects of fine-scale ($\approx 10^{-6}\text{s}$) thermal-hydraulics can be coupled to very-long-time scale processes, such as modeling corrosion ($\approx \text{months}$), required for predicting Crud-Induced Power Shift and Crud-Induced Localized Corrosion.
2. *Multiphase flows.* Some progress has been reported in an initial implementation of an N -fluid solver for multi-phase flow. Simple proof-of-concept simulations, with-

out phase-coupling at this time, demonstrate the potential to tackle various CASL challenge problems.

3. *Automatic mesh generation for very complex domains.* Numeca’s Hexpress/Hybrid mesh generator, a.k.a. “Spider”, has been used for the first time to generate computational meshes for computational problems in the nuclear engineering industry, in particular, for the GTRF problem. Spider is easy to use, fast, and automatically generates high-quality meshes with optional power-law-graded boundary layers. Output is saved in the latest HDF5/ExodusII format, capable of storing meshes in the billion-cell range. In the future, Spider will also be used to generate meshes for both the fluid and structural regions of a computational domain, targeted for fluid-structure interaction and conjugate heat transfer problems [20].
4. *New GTRF flow calculations.* A series of turbulent flow simulations have been carried out on both 3×3 and 5×5 rod bundle geometries. Various statistics of the fluctuating flow field have been analyzed and compared to data from computations carried out by Westinghouse using Star-CCM+ and from experiments at Texas A&M University. More details are given in [1].

ACKNOWLEDGMENTS

This research has been supported by the Consortium for Advanced Simulation of Light Water Reactors,⁴ a U.S. Department of Energy Innovation Hub⁵ under contract No. DE-AC05-00OR22725 (INL/CON-12-28011). Accordingly, the U.S. Government retains a non-exclusive, royalty-free license to publish or reproduce the published form of this contribution, or allow others to do so, for U.S. Government purposes.

REFERENCES

- [1] J. Bakosi, M.A. Christon, R.B. Lowrie, L.A. Pritchett-Sheats, and R.R. Nourgaliev. Large-Eddy Simulations of Turbulent Flow for Grid-to-Rod Fretting in Nuclear Reactors. *Nuclear Engineering and Design*, 2013.
- [2] John B. Bell, Philip Colella, and Harland M. Glaz. A second-order projection method for the incompressible navier-stokes equations. *Journal of Computational Physics*, 85:257–283, 1989.
- [3] M.A. Christon, J. Bakosi, and R.B. Lowrie. Hydra-TH User’s Manual. Technical Report LA-UR 12-23181, Los Alamos National Laboratory, December 2011.
- [4] Mark A. Christon. Hydra-TH Theory Manual. Technical Report LA-UR 11-05387, Los Alamos National Laboratory, September 2011.
- [5] Mark A. Christon, Jozsef Bakosi, Nathan Barnett, Marianne M. Francois, and Robert B. Lowrie. Initial Assessment of Hydra-TH on Grid-to-Rod Fretting Problems (thm.cfd.p4.01). Technical Report LA-UR-11-07034, Los Alamos National Laboratory, 2011.
- [6] M. E. Conner, E. E. Dominguea-Otiveros, and Y. A. Hassan. Hydraulic benchmark data for pwr mixing vane grid. In *The 14th International Topical Meeting on Nuclear Reactor Thermal Hydraulics*, Toronto, Canada, September 2011.

⁴<http://www.casl.gov>

⁵<http://www.energy.gov/hubs>

- [7] T. Dinh, R. Nourgaliev, and T. Theofanous. Understanding the ill-posed two-fluid model. In *The 10th International Topical Meeting on Nuclear Reactor Thermal Hydraulics*, 2003.
- [8] D. A. Drew and S. L. Passman. *Theory of multicomponent fluids*. Springer-Verlag, 1998.
- [9] A. M. Elmahdi, R. Lu, M. E. Conner, Z. Karoutas, and E. Baglietto. Flow induced vibration forces on a fuel rod by les cfd analysis. In *The 14th International Topical Meeting on Nuclear Reactor Thermal Hydraulics (NURETH-14)*, Hilton Toronto Hotel, Toronto, Ontario, Canada, September 2011.
- [10] Ercan Erturk and Bahityar Dursun. Numerical solutions of 2-d steady incompressible flow in a driven skewed cavity. *ZAMM - Journal of Applied Mathematics and Mechanics*, 87:377–392, 2007.
- [11] U. Ghia, N. Ghia, and C. T. Shin. High-*Re* solutions for incompressible flow using the Navier-Stokes equations and a multigrid method. *Journal of Computational Physics*, 48:387–411, 1983.
- [12] P. M. Gresho and R. L. Sani. *Incompressible flow and the finite element method, Advection-diffusion and isothermal laminar flow*. John Wiley & Sons, Chicester, England, 1998.
- [13] Philip M. Gresho. On the theory of semi-implicit projection methods for viscous incompressible flow and its implementation via a finite element method that also introduces a nearly consistent mass matrix. part 1: Theory. *International Journal for Numerical Methods in Fluids*, 11:587–620, 1990.
- [14] Philip M. Gresho and Stevens T. Chan. On the theory of semi-implicit projection methods for viscous incompressible flow and its implementation via a finite element method that also introduces a nearly consistent mass matrix. part 2: Implementation. *International Journal for Numerical Methods in Fluids*, 11:621–659, 1990.
- [15] Philip M. Gresho and Robert L. Sani. On pressure boundary conditions for the incompressible navier-stokes equations. *International Journal for Numerical Methods in Fluids*, 7:1111–1145, 1987.
- [16] M. Ishi and T. Hibiki. *Thermo-fluid dynamics of two-phase flow*. Springer-Verlag, 2011.
- [17] D. A. Knoll and D. Keyes. Jacobian-free Newton-Krylov methods: A survey of approaches and applications. *Journal of Computational Physics*, 193:357–397, 2004.
- [18] B. E. Launder and D. B. Spalding. The numerical computation of turbulent flows. *Comput. Meth. Appl. Mech. Eng.*, 3:269–289, 1974.
- [19] F. Nicoud and F. Ducros. Subgrid-scale stress modelling based on the square of the velocity gradient tensor. *Flow, Turbulence and Combustion*, 62:183–200, 1999. 10.1023/A:1009995426001.
- [20] Numeca Inc. personal communication. July 2012.
- [21] P.R Spalart and S. R. Allmaras. A one-equation turbulence model for aerodynamic flows. *La Recherche Aerospatiale*, 1:5–21, 1994.

- [22] P.R Spalart, W.H. Jou, M. Strelets, and S. R. Allmaras. Comments on the feasibility of LES for wings and on a hybrid RANS/LES approach. In *First AFOSR International Conference on DNS/LES*, Ruston Louisiana, 4-8 Aug 1997. Greyden Press.
- [23] H. Stadtke. *Gasdynamic Aspects of two-phase flow. Hyperbolicity, Wave Propagation Phenomena and Related Numerical Methods*. Wiley-VCH, 2006.
- [24] Shuangzhang Tu and Shahrouz Aliabadi. Development of a hybrid finite volume/element solver for incompressible flows. *International Journal for Numerical Methods in Fluids*, 20:177–203, 2007.
- [25] Shuangzhang Tu, Shahrouz Aliabadi, Reena Patel, and Marvin Watts. An implementation of the spalart-allmaras des model in an implicit unstructured hybrid finite volume/element solver for incompressible turbulent flow. *International Journal for Numerical Methods in Fluids*, 30:1051–1062, 2009.
- [26] Tian Wan, Shahrouz Aliabadi, and Christopher Bigler. A hybrid scheme based on finite element/volume methods for two immiscible fluid flows. *International Journal for Numerical Methods in Fluids*, 61:930–944, 2009.
- [27] J. Yan. personal communication. August 2012.
- [28] J. Yan, M. E. Conner, R. A. Brewster, Z. E. Karoutas, E. E. Dominguez-Ontiveros, and Y. A. Hassan. Validation of CFD method in predicting steady and transient flow field generated by PWR mixing vane grid. In *CFD4NRS-4 – The Experimental Validation and Application of CFD and CMFD Codes in Nuclear Reactor Technology, OECD/NEA & International Atomic Energy Agency (IAEA) Workshop*, Daejeon, Korea, September 2012.

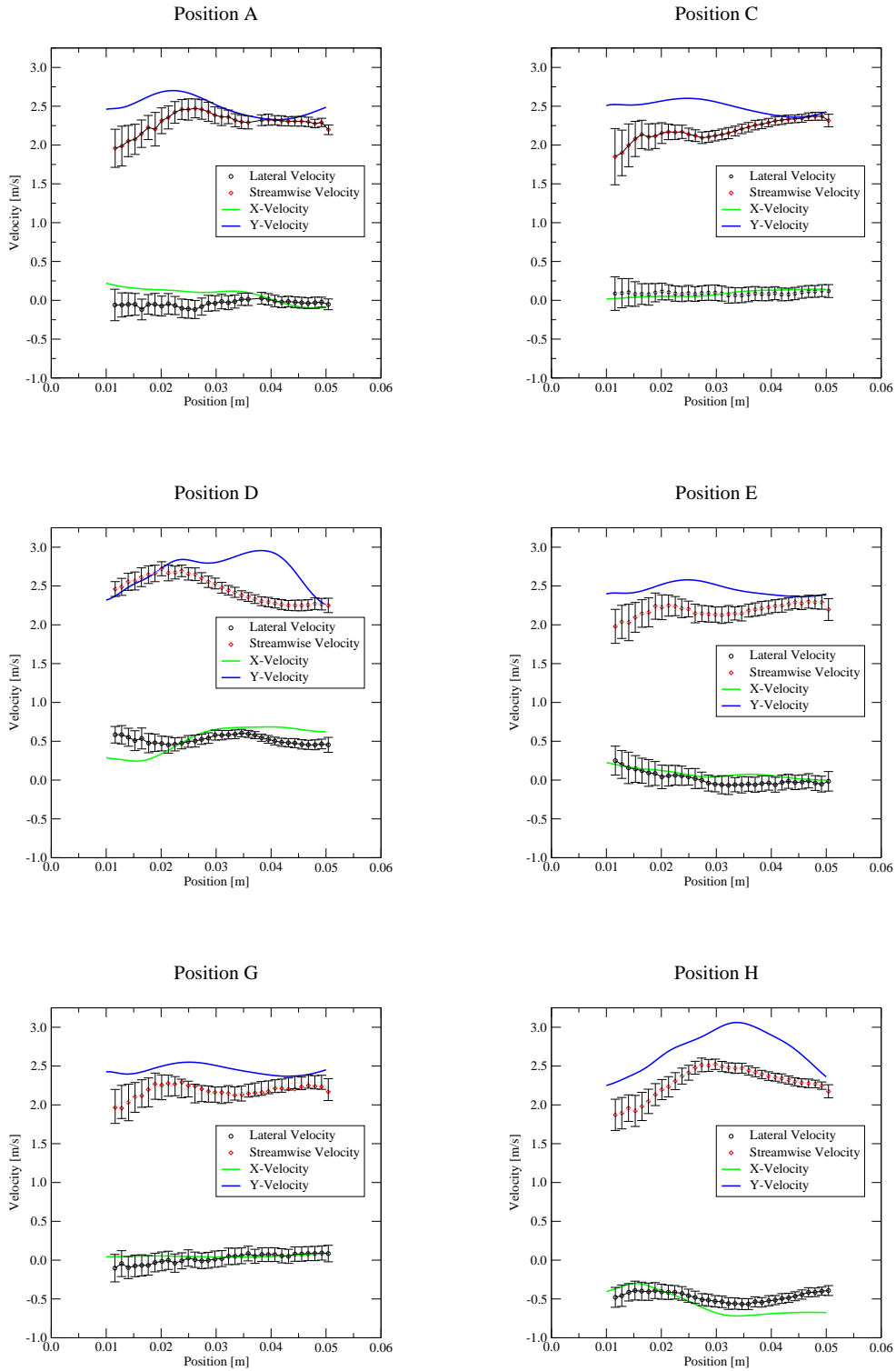


Fig. 16: Mean axial and lateral velocity profiles at positions A, C, D, E, G and H for the 96M mesh.

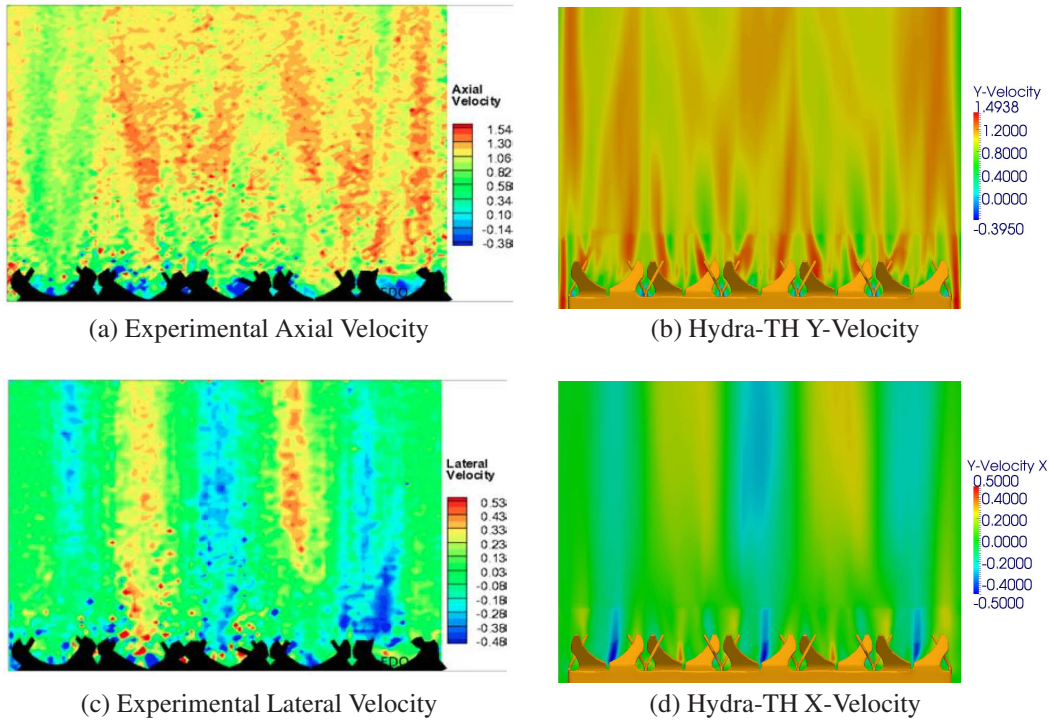


Fig. 17: Experimental and computed axial (y-direction) time-averaged velocities on plane 5. Velocity magnitude has been scaled relative to the 2.48 m/s inlet velocity.

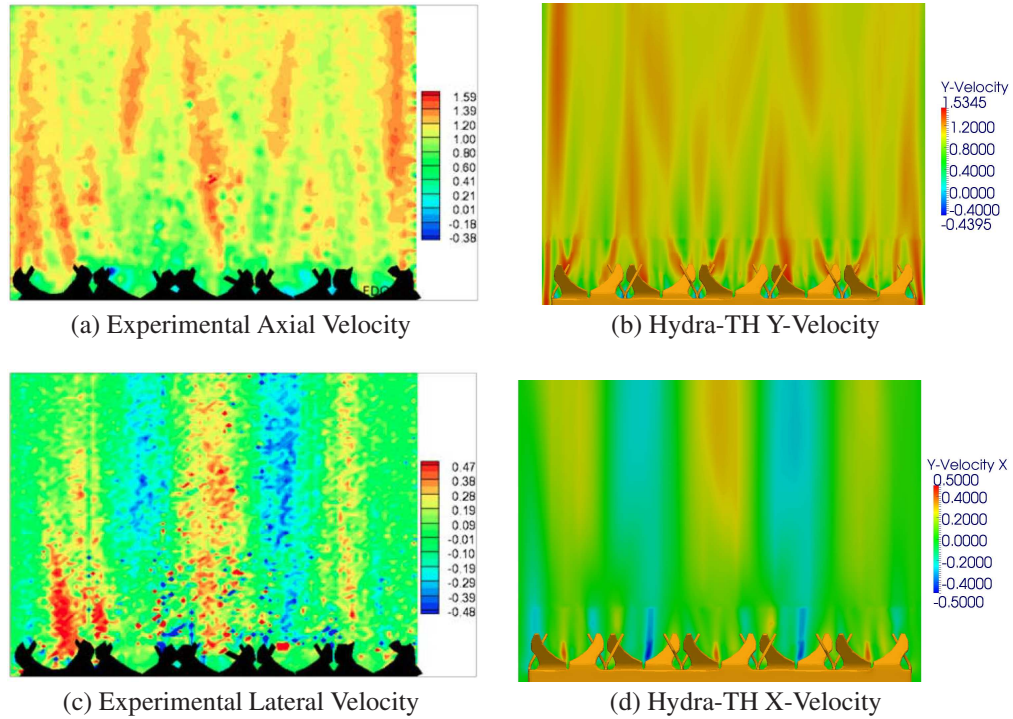


Fig. 18: Experimental and computed axial (y-direction) time-averaged velocities on plane 7. Velocity magnitude has been scaled relative to the 2.48 m/s inlet velocity.